Effects of cooperative diffusion on rheological and mechanical behavior of bcc Fe: A combined approach using elastically collective nonlinear Langevin equation theory and statistical moment method

Tran Dinh Cuong [1,*] and Anh D. Phan [1,2]

[1] *Faculty of Materials Science and Engineering, Phenikaa University, Yen Nghia, Ha Dong, Hanoi 12116, Vietnam*
[2] *Phenikaa Institute for Advanced Study (PIAS), Phenikaa University, Yen Nghia, Ha Dong, Hanoi 12116, Vietnam*

(Received 11 October 2023; revised 25 January 2024; accepted 26 January 2024; published 21 February 2024)

Anomalous seismic data on Earth's inner core have challenged our understanding of mineral physics for decades. According to recent *ab initio* studies, bcc Fe may be a key to solving this long-standing problem. However, simulating the bcc phase requires an enormous supercell, a long simulation time, and a prohibitive computational cost. Consequently, available information about bcc Fe is very limited. Herein, we introduce a more convenient approach for investigating the rheological and mechanical properties of the bcc structure under deep-Earth conditions. Since bcc Fe behaves similarly to a liquid system while remaining within the solid state, we treat it as a hard-sphere glass former in the elastically collective nonlinear Langevin equation theory. On that basis, we can readily evaluate the contribution of local and nonlocal interactions to the motion of atoms at various packing fractions. To consider finite-temperature and hydrostatic-pressure effects, we utilize the statistical moment method. The mentioned strategy enables us to determine the diffusivity, viscosity, and rigidity of bcc Fe without strenuous computational efforts. In addition, we discover a close connection between the glass and superionic transitions. Our theoretical calculations agree quantitatively well with cutting-edge large-scale molecular dynamics simulations. Therefore they would be valuable for unlocking the mysteries of Earth's inner core, such as the low shear resistance, the high Poisson ratio, and the strong seismic-wave attenuation.

DOI: 10.1103/PhysRevB.109.054112

I. INTRODUCTION

Earth's inner core (IC) has become one of the most fascinating research topics for geophysicists since 1936 [1–3]. Although this small solid ball currently occupies less than 1% of the volume of our home planet [4], it profoundly affects Earth's dynamics, evolution, and habitability [5]. Specifically, the slow but continuous growth of the IC promotes the vigorous convection of liquid alloys in Earth's outer core (OC) by releasing fusion enthalpies and light elements [6]. This mechanism is chiefly responsible for powering and maintaining the magnetosphere, which protects living creatures from fatal solar winds [7]. Besides, the heat extracted from Earth's core is a crucial energy source for the fluidlike circulation of the silicate mantle [8]. It should be stressed that mantle convection plays an essential role in driving geological processes at Earth's surface, such as plate tectonics, earthquakes, erosion, and volcanism [9–11].

The above results have motivated a host of investigations into minerals under extreme pressure-temperature (P-T) conditions to yield a deeper insight into the geophysical properties of the IC [12–14]. In that context, Fe is considered the leading object of study because this transition metal makes up more than 80% of the weight of Earth's core [15]. Accurate information about the stability, rheology, and elasticity of Fe is indispensable for elucidating the past, present, and future of the IC as well as the Earth [16–19].

The prevailing view among geophysicists is that the most stable structure of Fe in the IC environment ($P = 330-360$ GPa and $T = 5000-7000$ K) is the hcp lattice [20–23]. On the computational side, this point of view has been actively supported by the substantial body of *ab initio* calculations. Based on the *ab initio* thermodynamic integration (AITI) and the *ab initio* molecular dynamics (AIMD), González-Cataldo and Militzer [24] demonstrated that hcp Fe would have the lowest Gibbs energy among possible polymorphs in a pressure interval from 300 to 5000 GPa. Their findings were highly consistent with the quantum-mechanical simulations of Vocadlo *et al.* [25], Sun *et al.* [26], Wu *et al.* [27], and Kruglov *et al.* [28]. Notably, Zhang *et al.* [29] discovered the strong collective motion of Fe atoms in the premelting region of the hcp phase by combining the AIMD and the machine-learning molecular dynamics (MLMD). This exciting phenomenon helped explain the strange mechanical responses of the IC satisfactorily [29]. On the experimental side, both static and dynamic data have shown the stability of hcp Fe in planetary cores. Relying on the extended x-ray absorption fine structure spectroscopy, Ping *et al.* [30] observed the appearance of an 11-coordinated phase in shock-compressed Fe samples from 90 to 560 GPa. This coordination number aligned with the formal atomic arrangement of hcp Fe with 12 nearest neighbors per site [30]. Likewise, Kraus *et al.* [31] performed x-ray diffraction measurements on ramp-compressed Fe systems, and they only detected the

*cuong.trandinh@phenikaa-uni.edu.vn

melting signatures of the hcp structure between 300 and 1000 GPa. The dominance of hcp Fe had also been confirmed by the diamond-anvil-cell (DAC) experiments of Boehler *et al.* [32], Anzellini *et al.* [33], and Sinmyo *et al.* [34] despite great uncertainty about the location of melting points T_m.

However, using hcp Fe alone is insufficient to model the IC interior. The situation leads to an intriguing hypothesis that the IC may simultaneously contain hcp and bcc phases [35–37]. Even though the intrinsic stability of bcc Fe is very controversial [38–41], this material still has a chance to exist in the IC for the following three reasons. First, it is well-known that the solid IC is formed via the bottom-up crystallization of the liquid OC [2]. Yet, liquid Fe is unlikely to transform into hcp Fe directly because this process necessitates an impractical degree of undercooling (about 1000 K) [42]. A more reasonable hypothesis is to consider that the nucleation occurs via the two-step scenario of Sun *et al.* [43] as liquid→bcc→hcp. Hence, there is a possibility that bcc Fe would appear within the metastable state under IC conditions [35]. Second, apart from Fe, the IC also contains a significant amount of S, Si, and Ni [15]. These chemical elements are often viewed as a bcc stabilizer in terms of thermodynamics [44,45]. Namely, Ozawa *et al.* [46] indicated that Fe-S alloys would decompose into bcc and hcp parts at $P \geqslant 250$ GPa. A similar picture was also found in the subsequent DAC investigations into Fe-Si binaries of Tateno *et al.* [47]. In that spirit, Ikuta *et al.* [48] continued to investigate Fe-Ni-Si ternary alloys via the DAC technique, thereby highlighting the decomposition of these systems to hcp-bcc mixtures in harsh P-T environments. The mentioned experiments [46–48] have received considerable support from various *ab initio* calculations [49–51]. Thus the thermodynamically stable coexistence of hcp and bcc structures is a possibility that should be carefully considered when modeling the IC interior. Third, the bcc inclusion promises to open a fruitful avenue for deciphering Earth's enigmas. For instance, it is viable to utilize the bcc phase to deal with the nucleation paradox [43], the hemispherical dichotomy [37], the elastic anisotropy [36], and the structural complexity [35] of the IC. Additionally, since bcc Fe possesses the unique features of both crystalline and molten metals [52], its appearance would be beneficial to answer why the IC exhibits sharp seismic attenuation and poor shear resistance [53].

These remarkable discoveries have sparked a strong interest in bcc Fe in the geophysical community. One can readily find valuable information about its thermodynamic, electronic, and magnetic characteristics in the recent *ab initio* reports of Bouchet *et al.* [54], Pourovskii *et al.* [55], and Gambino *et al.* [56]. Relevant machine-learning outputs are also publicly accessible via the works of Ghosh *et al.* [57] and Brannvall *et al.* [58]. Therefore the remaining issue is to illuminate the liquid-like rheological and mechanical behaviors of bcc Fe. According to Belonoshko *et al.* [59,60], the above behaviors are mainly decided by the superionic self-diffusion of Fe atoms in the bcc lattice. An enormous supercell with at least 1024 atoms is required to generate and maintain the superionic state in bcc Fe [39,41], where the sliding of crystallographic planes is analogous to shuffling a deck of cards. If not, the bcc architecture will be rapidly destroyed by deviatoric stresses [39,41]. More seriously, one may need to scrutinize millions of atoms over a long period to reach the convergence of physical quantities [59]. These demanding requirements make the simulation of diffusivity, viscosity, and elasticity arduous. For example, to unambiguously determine the AIMD elastic constants of bcc Fe at Earth's center, Belonoshko *et al.* [60] used 16 fat nodes with a memory of 384 GB at the Tetralith—the most powerful supercomputer cluster in Sweden. Despite possessing state-of-the-art computational tools, they still had to make a massive investment of time and effort in completing their project [60]. Up to five weeks of computer time were necessitated to capture the mechanical response of a 2000-atom supercell to each applied strain [60]. As an inevitable consequence, available data on superionic bcc Fe remains particularly scarce while they are vital for designing geodynamic models.

Herein, we aim to improve this predicament by developing a combined theoretical approach for reliably predicting the liquid-like behaviors of bcc Fe at minimal computational expense. Our ideas originate from an intimate connection between a superionic crystal and a glass former. Fundamentally, both of them are intermediate between solid and liquid. Hence, their physical properties are expected to be much the same. Indeed, Gray-Weale and Madden [61,62] pointed out numerous phenomenological resemblances between fluorite-structured superionic conductors and atomic-disordered supercooled liquids, such as the violation of Arrhenius's law [63] for transport coefficients, the presence of abnormal peaks in heat-capacity profiles, the two-step relaxation of time-correlation functions, and the validity of the Adam-Gibbs model [64] for mobility-entropy relationships. Zhang *et al.* [65,66] also achieved the same conclusion after carrying out classical molecular dynamics simulations on UO_2 with the embedded atom method (EAM). Besides, the vitrification and superionic temperatures are very close to each other. Phan *et al.* [67] applied machine-learning algorithms to about 100 amorphous pharmaceuticals and saw that they would be vitrified at $T \approx T_m/1.4$. An identical trend was also found in semiempirical investigations into halide and oxide compounds, where the superionic transition would typically occur at $T \approx T_m/1.3$ [68–70]. These results have offered us an attractive prospect of dealing with complicated problems about superionicity via available knowledge of glassy dynamics.

It is worth noting that the underlying physics of glass-forming substances can be quantitatively understood via the elastically collective nonlinear Langevin equation (ECNLE) theory [71–74]. In the ECNLE, a hard-sphere fluid is utilized as a general reference system for every material [71,72]. On that basis, scientists can readily analyze the impact of local and collective interactions on the structural relaxation of molecules at various time scales (from picosecond to hectosecond) [71,72]. Specific information about the studied object (e.g., molar mass and particle diameter) is encoded in a chemical mapping [73,74], which converts the packing fraction Φ to the hydrostatic pressure P and the absolute temperature T. The success of the ECNLE has been continuously recorded in many cases, including thermal liquids [75], polymer melts [76], amorphous drugs [77], glassy graphene [78], and metallic glasses [79]. These impressive achievements motivate us to extend the ECNLE to bcc Fe. To construct the chemical mapping, we adopt the statistical moment method (SMM) and the work-heat equivalence

principle (WHEP) [80]. The most prominent advantage of the SMM-WHEP is that we can directly deduce the high-pressure melting boundaries of metals from their room-temperature equation-of-state (EoS) parameters without onerous computational processes [80]. Our theoretical calculations for bcc Fe are comprehensively compared with cutting-edge simulations and experiments. Their geophysical implications for the IC are also discussed in detail.

II. THEORETICAL BACKGROUND

A. ECNLE reference system

The essence of the ECNLE is sketched in Fig. 1. As introduced in the first section, any supercooled or superionic material can be mapped to an assembly of countless rigid spheres having the diameter σ and the density $\rho = 6\Phi\pi^{-1}\sigma^{-3}$ in the ECNLE [71,72]. To rapidly describe the spatial arrangement of these spheres, we employ the well-known Percus-Yevick approximation [81]. Namely, the direct correlation function $C(r)$ is explicitly expressed by [82]

$$C(r) = \left\{3\Phi(2+\Phi)^2\frac{r}{\sigma} - (1+2\Phi)^2\left[\Phi\left(\frac{r}{\sigma}\right)^3 + 2\right]\right\} \times \frac{\Theta(\sigma - r)}{2(1-\Phi)^4}, \tag{1}$$

where $\Theta(\sigma - r)$ is the Heaviside step function. Applying the Fourier transform to Eq. (1) gives us

$$C(q) = \frac{4\pi}{q}\int_0^\sigma C(r)\sin(qr)rdr, \tag{2}$$

where q is the wavevector. Based on Eq. (2), it is feasible to calculate the static structure factor $S(q)$ and the radial distribution function $g(r)$ by [83]

$$S(q) = \frac{1}{1-\rho C(q)},$$
$$g(r) = 1 + \frac{1}{2\pi^2\rho r}\int_0^\infty [S(q)-1]q\sin(qr)dq. \tag{3}$$

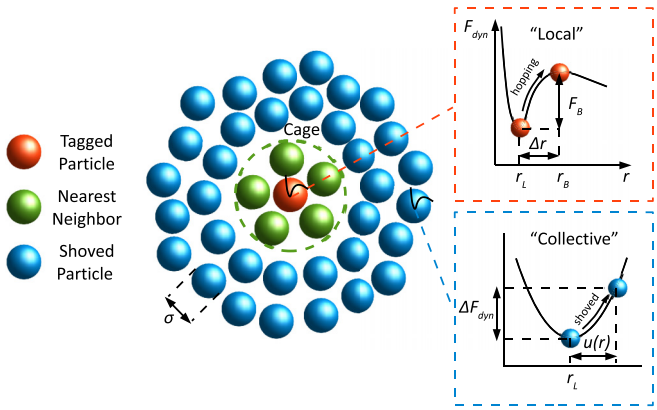

FIG. 1. Illustration of the ECNLE reference system. Each atom corresponds to a hard sphere whose motion is controlled by the dynamic free energy $F_{\rm dyn}$. When the tagged particle hops out of its neighboring cage owing to the thermally activated event, it triggers a long-range harmonic displacement field in the surrounding fluid.

Interestingly, according to Khrapak *et al.* [84], we can infer the instantaneous shear modulus G from Eq. (3) as follows:

$$G = \rho k_B T\left[1 - \frac{8}{5}\Phi\sigma\lim_{\epsilon\to 0^+}\left(\frac{dg}{dr}\right)_{r=\sigma(1+\epsilon)}\right], \tag{4}$$

where the first and second terms represent kinetic and configurational contributions, respectively. For more convenience, Eq. (4) is rewritten by

$$G = \rho k_B T\left[1 + \frac{36}{5}\frac{\Phi^2(1+\Phi)}{(1-\Phi)^3}\right], \tag{5}$$

where k_B symbolizes the Boltzmann constant.

To consider the molecular mobility of the aforeconstructed system, we adopt the nonequilibrium free-energy method of Schweizer *et al.* [85–87]. Specifically, the interaction between an arbitrarily tagged particle and its surroundings is characterized by a dynamic quantity $F_{\rm dyn}$ as

$$F_{\rm dyn} = F_{\rm ideal} + F_{\rm excess}. \tag{6}$$

From a physical perspective, $F_{\rm ideal}$ arises from the short-time Fickian diffusion and promotes the delocalized fluid state. In contrast, $F_{\rm excess}$ denotes an entropic trapping potential, which facilitates localization. Their analytical expressions are provided by [85–87]

$$F_{\rm ideal} = -3k_BT\ln\frac{r}{\sigma}, \tag{7}$$

$$F_{\rm excess} = -k_BT\int\frac{d\vec{q}}{(2\pi)^3}\frac{\rho C^2(q)S(q)}{1+S^{-1}(q)}e^{-\frac{1}{6}q^2r^2[1+S^{-1}(q)]}. \tag{8}$$

Figure 1 shows how $F_{\rm dyn}$ affects the motion of the tagged particle. At $\Phi < 0.432$, since $F_{\rm ideal}$ overwhelms $F_{\rm excess}$, $F_{\rm dyn}$ undergoes a monotonical reduction with increasing r [85–87]. This tendency implies that the tagged particle can readily diffuse without kinetic constraints in dilute solutions. However, when our system is dense enough ($\Phi \geqslant 0.432$), a finite-potential well with a depth of F_B emerges in the dynamic free-energy profile due to the enhancement of trapping effects [85–87]. Accordingly, the tagged particle is temporarily confined in a local cage created by its nearest neighbors. For simplicity, the cage radius $r_{\rm cage}$ is approximated to be 1.5σ [78]. The localization length r_L and the barrier position r_B are determined by numerically solving the extremum condition of $F_{\rm dyn}$. From there, the local barrier height F_B is given by [85–87]

$$F_B = F_{\rm dyn}(r_B) - F_{\rm dyn}(r_L). \tag{9}$$

After getting confined, the tagged particle tries to escape from confinement via thermally activated hopping processes [71,72]. It should be noted that the jump distance $\Delta r = r_B - r_L$ is quite long on the cage scale. For instance, Δr can be up to 0.412σ at $\Phi = 0.64$. Thus this escape perturbs the surrounding fluid by generating a long-range distortion field [71,72]. To quantify the displacement $u(r)$ of particles outside the cage, we use the Landau-Lifshitz continuity equation as [88]

$$u(r) = \Delta r_{\rm eff}\left(\frac{r_{\rm cage}}{r}\right)^2, \tag{10}$$

where $\Delta r_{\rm eff} \approx 0.09375\Delta r^2 r_{\rm cage}^{-1}$ indicates the expansion of the first coordination shell [71,72]. Because $u(r)$ is much smaller than r_L, it is reasonable to treat each shoved particle as a harmonic oscillator with the Hooke constant $K_L = (\partial^2 F_{\rm dyn}/\partial r^2)_{r=r_L}$ and the free-energy change $\Delta F_{\rm dyn} = K_L u^2(r)/2$. This treatment helps us to quickly calculate the total strain energy F_E stored in the remaining elastic medium by [71,72]

$$F_E = \int_{r_{\rm cage}}^{\infty} 4\pi r^2 \rho g \Delta F_{\rm dyn} dr \approx 12\Phi\Delta r_{\rm eff}^2 \left(\frac{r_{\rm cage}}{\sigma}\right)^3 K_L, \tag{11}$$

where $g(r) \approx 1$ for $r \geqslant r_{\rm cage}$.

Now, it is conspicuous that the tagged particle needs to overcome not only the local barrier F_B but also the collective barrier F_E to break out of the cage. The role of F_B and F_E in structural relaxation crucially depends on the packing fraction Φ of the system. As demonstrated by Mirigian and Schweizer [71,72], F_E is essentially negligible compared to F_B at $\Phi < 0.55$. Nevertheless, when Φ exceeds 0.57, the growth rate of F_E becomes significantly faster than that of F_B. This event leads to the dominance of collective dynamics near the glass transition point ($\Phi^* \approx 0.611$) and explains why glass formers exhibit non-Arrhenius behaviors during isobaric cooling [71,72]. The mechanism is most likely also valid for superionic crystals [65,66]. Relying on the above arguments, we can estimate the average time for escape or the so-called structural relaxation time τ_α via the modified Kramers theory as [71,72]

$$\tau_\alpha = \tau_s \left[1 + \frac{2\pi}{\sqrt{K_L K_B}} \frac{k_B T}{\sigma^2} \exp\left(\frac{F_B + F_E}{k_B T}\right)\right], \tag{12}$$

where $K_B = -(\partial^2 F_{\rm dyn}/\partial r^2)_{r=r_B}$. Details about τ_s were extensively reported in earlier ECNLE works [89–91].

Equation (12) enables us to investigate the rheology of the hard-sphere fluid at different time scales spanning from picosecond to hectosecond [71,72]. Indeed, the time dependence of the mean square displacement $\langle r^2(t)\rangle$ of the tagged particle is described by

$$\langle r^2(t)\rangle = \frac{\Delta r^2}{\tau_\alpha} t. \tag{13}$$

Similar to AIMD and quasi-AIMD simulations [59], the diffusivity D is defined by

$$D = \lim_{t\to\infty}\left[\frac{\langle r^2(t)\rangle}{6t}\right] = \frac{\Delta r^2}{6\tau_\alpha}. \tag{14}$$

Notably, Belonoshko *et al.* [59] indicated that the diffusion of Fe atoms in the bcc phase would be fully Brownian over a long interval. This indication suggests that we can compute the viscosity η by the Stokes-Einstein relation [92,93] instead of the Green-Kubo formula [94,95] to save computational costs. Therefore η is directly associated with D via

$$\eta = \frac{k_B T}{2\pi\sigma D}. \tag{15}$$

Numerical results derived from Eqs. (5), (12), (14), and (15) are tabulated in the Appendix A. Emphasize again that these results are universal. Applying them to a specific substance necessitates an appropriate chemical mapping [73,74]. So, how do we satisfy this requirement? A detailed answer is presented in the subsequent section.

B. SMM-WHEP chemical mapping

Overall, there are two ways to link the ECNLE reference system to an actual material.

(1) Constructing Schweizer's mapping. In pioneering ECNLE works, Schweizer *et al.* [73] equated the Percus-Yevick dimensionless compressibility with its experimental counterpart to represent Φ as a function of P and T. This strategy succeeded in capturing the glassy dynamics of numerous thermal liquids [75] and polymer melts [76]. Notwithstanding, Schweizer's approach [73] is inapplicable in the current situation. The primary reason is that EoS data for bcc Fe in the superionic state are unavailable. As mentioned in the introduction, conducting AIMD investigations into bcc Fe is a grand challenge in the extreme P-T domain [39,41,59,60]. Consequently, we do not have enough information about the isothermal compressibility of the superionic phase to build Schweizer's mapping. Besides, the analytical expression for $\Phi(P,T)$ [73] is quite bulky. It should be restressed that our ultimate goal is to get a reliable description of bcc Fe with minimal computational efforts. In that spirit, all mathematical aspects of our theoretical model need to be as simple as possible.

(2) Constructing Phan's mapping. Lately, Phan *et al.* [74] proposed a more viable solution for converting ECNLE outputs from the Φ space to the P-T one. Their principal idea came from the thermal dilation of glass-forming liquids during isobaric heating. On that basis, Phan *et al.* successfully deciphered the structural relaxation of amorphous pharmaceuticals [77], graphene melts [78], and metallic glasses [79] under various thermodynamic conditions, even when the EoS parameters of these materials were entirely unknown. Their ECNLE calculations were not only physically understandable but also mathematically straightforward [77–79]. Hence, the conversion from Φ to P and T merely took a few minutes on a personal computer. The above advantages make Phan's method [74] the most suitable choice for our research.

In the case of bcc Fe, we have

$$\Phi(P,T) = \Phi_0\{1 - \beta(P)[T - T_0(P)]\}, \tag{16}$$

where Φ_0 is the initial packing fraction, T_0 is the initial temperature, and β is the volumetric expansivity α times the scaled particle density $\rho\rho_0^{-1}$. It is clear to see that T_0 is associated with the superionic temperature T^* via

$$T_0(P) = T^*(P) + \frac{1}{\beta(P)}\frac{\Phi^* - \Phi_0}{\Phi_0}. \tag{17}$$

Inserting Eq. (17) into Eq. (16) creates

$$\Phi(P,T) = \chi(P)[T^*(P) - T] + \Phi^*, \tag{18}$$

where $\chi = \Phi_0\beta = \pi\rho_0\sigma^3\beta/6$. Because σ only drops slightly from 2.57 Å at 0 GPa [96] to 2.40 Å at 360 GPa [52], we set $\sigma = 2.57$ Å throughout our analyses. Eq. (18) denotes the final form of Phan's mapping. This expression works best in a P-T area enclosed by bcc-liquid and hcp-bcc boundaries.

Accordingly, our task is to find how T_m and T^* vary under hydrostatic compression.

Let us start with T_m first. To determine the melting properties of bcc Fe, we utilize the SMM-WHEP scheme of Cuong and coworkers [80]. The SMM-WHEP scheme is built on the fact that both mechanical deformation and heat absorption can cause the liquefaction of crystals by breaking down chemical bonds [97]. In other words, the work done when expanding along isotherms and the heat absorbed when dilating along isobars are equivalent [98–100]. This principle allows us to access the high-pressure melting curve of metals via their room-temperature EoS as [80]

$$T_m(P) = T_1(P_1) + [T_2(P_2) - T_1(P_1)]\sqrt{\frac{\int_{\xi_1}^{\xi} P_{300\mathrm{K}}(\xi')\xi'^2 d\xi'}{\int_{\xi_1}^{\xi_2} P_{300\mathrm{K}}(\xi')\xi'^2 d\xi'}},$$
$$\xi = \xi'(P, 300\,\mathrm{K}),\ \xi_1 = \xi'(P_1, 300\,\mathrm{K}),$$
$$\xi_2 = \xi'(P_2, 300\,\mathrm{K}), \tag{19}$$

where $T_1(P_1)$ and $T_2(P_2)$ stand for two reference melting points. To simplify EoS-related integrals, we employ the Vinet parametrization method [101], which is

$$P_{300\mathrm{K}}(\xi') = 3B_0\xi'^{-2}(1-\xi')e^{\frac{3}{2}(B_0'-1)(1-\xi')}. \tag{20}$$

Whereas ξ' is the cube root of the normalized atomic volume, B_0 and B_0' are the isothermal bulk modulus and its partial derivative to pressure at standard conditions. Entering Eq. (20) into Eq. (19) gives us

$$T_m(P) = T_1(P_1) + [T_2(P_2) - T_1(P_1)]\sqrt{\frac{W(\xi) - W(\xi_1)}{W(\xi_2) - W(\xi_1)}},$$
$$W(\xi) = \left[1 + \frac{3}{2}(B_0' - 1)(\xi - 1)\right]e^{\frac{3}{2}(B_0'-1)(1-\xi)}. \tag{21}$$

The accuracy of Eq. (21) was validated for benchmark metals whose melting lines were unambiguously reported up to hundreds of gigapascals [80] (e.g., Al, Cu, and V). Especially for hcp Fe, the SMM-WHEP [80] was proven to outperform conventional semiempirical models (e.g., the Lindemann law [102] and the Burakovsky theory [103]). To apply Eq. (21) to bcc Fe, we extract $P_1 = 0$ GPa, $P_2 = 5.2$ GPa, $T_1 = 1811$ K, and $T_2 = 1991$ K from the well-established low-pressure phase diagram of Swartzendruber [104]. In addition, $B_0 = 198.76$ GPa and $B_0' = 5.05$ are deduced from solving the force balance criterion with the moment recurrence technique in quantum statistical mechanics [105–107]. The quality of these Vinet parameters is verified in Appendix B.

Figure 2 depicts the impact of P on the growth of T_m. Experimentally, the existing data are strongly scattered, but we can categorize them into three principal groups: (i) low-T_m, (ii) intermediate-T_m, and (iii) high-T_m [Fig. 2(a)]. Group (i) chiefly consists of the DAC data of Boehler *et al.* [32], Aquilanti *et al.* [108], and Basu *et al.* [109], where T_m is expected to reach 4850 K at the OC-IC interface. Meanwhile, group (ii) is constructed from the DAC measurements of Jackson *et al.* [110], Zhang *et al.* [111], and Sinmyo *et al.* [34], where T_m is predicted to be ≈ 5700 K at the bottommost OC. This T_m value can increase by $\approx 250-700$ K if one considers experimental data in group (iii). Remark that group (iii) is the largest,

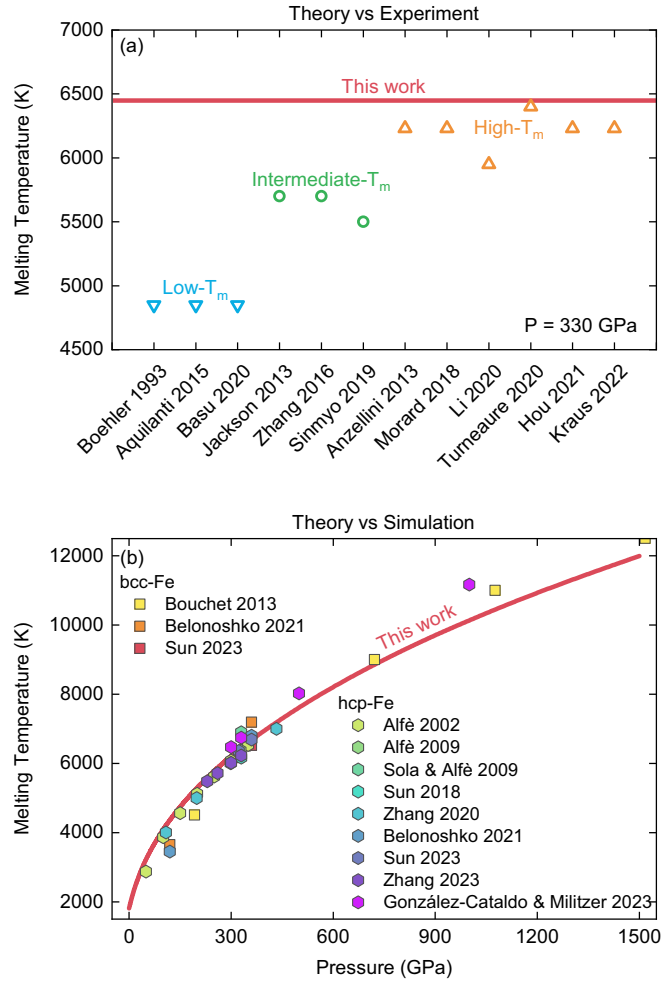

FIG. 2. Our theoretical calculations for the melting temperature of bcc Fe in comparison with previous experiments [31–34,108–115] (a) and simulations [24,26,29,41,54,116–120] (b).

retaining a vast body of information supplied by Anzellini *et al.* [33], Morard *et al.* [112], Li *et al.* [113], Turneaure *et al.* [114], Hou *et al.* [115], and Kraus *et al.* [31]. Moreover, group (iii) shows a concurrence between state-of-the-art static and dynamic experiments, which is absent in group (i) and group (ii). Thus it is widely believed that Fe would undergo the solid-liquid transition at high temperatures [31,33,112–115]. The low and intermediate melting points published in prior DAC papers [32,34,108–111] may stem from carbon contamination, plastic deformation, pressure overestimation, or chromatic aberration [112,115].

Sharing the opinion of experimentalists in group (iii) [31,33,112–115], most theorists recommend a steep melting curve for Fe [Fig. 2(b)]. Specifically, Eq. (21) indicates that T_m rises dramatically from 6452 K at 330 GPa to 11994 K at 1500 GPa. Our SMM-WHEP analyses agree quantitatively with earlier *ab initio* [24,26,54,116–119], quasi *ab initio* [41], and machine-learning [29,120] simulations. The relative error is less than 5% over most of the examined pressure range. This number confirms that Eq. (21) is sufficiently accurate to place the upper limit for the variable T in Phan's mapping.

Nevertheless, there is still an open question about the melting relation between hcp Fe and bcc Fe. Bouchet *et al.* [54] suggested that hcp and bcc architectures would be liquified under identical physical conditions. Unfortunately, their conclusion was drawn from the one-phase approach, so it may be incorrect owing to superheating phenomena. In contrast to the view of Bouchet *et al.* [54], Belonoshko *et al.* [41] believed the melting temperature of bcc Fe would be 6% higher than that of hcp Fe after performing quasi *ab initio* free-energy simulations on unprecedentedly large supercells with 16 000 000 atoms. Yet, their computational results remain debatable due to the limitations of the EAM potential. Recall that the EAM parameters of Belonoshko *et al.* [41] were derived from FPLMTO profiles at 0 K. An *ad hoc* correction was required to add the electronic entropy to the EAM free energy [41]. Therefore their EAM model may be unsuitable for clarifying the difference between T_m^{hcp} and T_m^{bcc} under the extreme heat of Earth's core. Unlike Bouchet *et al.* [54] and Belonoshko *et al.* [41], Sun *et al.* [26] argued that the bcc-liquid equilibrium line should sit below the hcp-liquid counterpart. The gap between these melting boundaries would narrow from 189 K at 323 GPa to 173 K at 360 GPa [26]. Although the AITI calculations of Sun *et al.* [26] included the contribution of both ions and electrons naturally, the finite-size problem was not fully addressed. Consequently, more efforts are necessary to settle the heated debate about the melting transition of Fe at elevated pressures.

Next, we turn our attention to T^*. On the experimental side, Hrubiak *et al.* [121] measured the variation of T^* during squeezing from 95 to 221 GPa by combining *in-situ* and spatially resolved x-ray diffraction methods. On the computational side, Belonoshko *et al.* [41] simulated the hcp-bcc structural transformation of Fe at 120 and 360 GPa by coupling the quasi-AIMD with the AIMD. A good agreement between experiments [121] and simulations [41] was achieved. That means we can exploit information from these studies [41,121] to describe the T^* versus P correlation. Conspicuously, the hcp-bcc coexistence points of Hrubiak *et al.* [121] and Belonoshko *et al.* [41] are well parametrized by the Simon-Glatzel law as [122]

$$T^*(P) = k_1\left(1+\frac{P}{k_2}\right)^{\frac{1}{k_3}}, \tag{22}$$

where $k_1 = 1293$ K, $k_2 = 17.17$ GPa, and $k_3 = 2.29$. By comparing Eqs. (21) and (22), we realize that the T_m-to-T^* ratio approximately equals 1.35 in the fitting interval between 95 and 360 GPa, consistent with the machine-learning predictions of Phan *et al.* [67].

More fascinatingly, it is practicable to deduce χ from T^*. Indeed, the pressure impact on the bulk dilation can be evaluated via the Dass-Kumari formula as [123]

$$\chi(P) = \frac{\chi(0)}{1+\frac{B_0^{*'}}{B_0^*}P.} \tag{23}$$

Here, B_0^* and $B_0^{*'}$ have the same physical meaning as B_0 and B_0', but they should be calculated at $T = k_1$ instead of $T = 300$ K. Relying on the dislocation-mediated phase-transition theory [103,124,125], we can link B_0^*, $B_0^{*'}$, and T^*

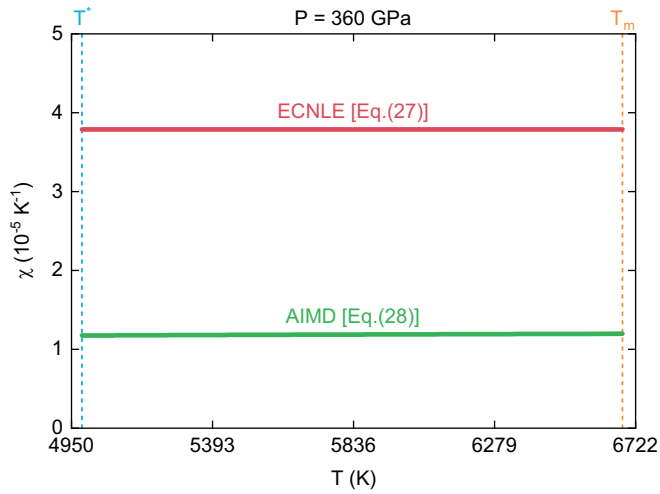

FIG. 3. ECNLE and AIMD estimations for the coefficient χ in Phan's mapping.

in the low-pressure regime as

$$T^*(P) \approx T^*(0)\left[1+\frac{B_0^{*'}-1}{B_0^*}P+\frac{1}{B_0^{*2}}\left(\frac{1}{2}-\frac{5}{6}B_0^{*'}\right)P^2\right]. \tag{24}$$

Simultaneously, by applying the Taylor-Maclaurin expansion [126] to the Simon-Glatzel law [122], we have

$$T^*(P) \approx k_1\left(1+\frac{1}{k_2k_3}P+\frac{1-k_3}{2k_2^2k_3^2}P^2\right). \tag{25}$$

Equating the coefficients of the above expressions results in

$$B_0^* = \frac{k_2k_3\left(\sqrt{1+24k_3}+5\right)}{6(k_3-1)},\ B_0^{*'} = \frac{6k_3+\sqrt{1+24k_3}-1}{6(k_3-1)}. \tag{26}$$

Continuing to enter Eq. (26) into Eq. (23) yields

$$\chi(P) \approx \frac{\chi(0)}{1+\frac{6k_3+\sqrt{1+24k_3}-1}{k_2k_3\left(\sqrt{1+24k_3}+5\right)}P}. \tag{27}$$

Equation (27) highlights an intimate connection between the intrinsic superionicity and the thermal expansivity. To ensure consistency with previous ECNLE works, we choose $\chi(0) = 6\times10^{-4}$ K^{-1}. The figure was obtained by fitting Eq. (18) to Schweizer's mapping for polystyrene, polycarbonate, polyisobutylene, and orthoterphenyl [75]. Due to the difficulty in gathering EoS data, Phan *et al.* [74] proposed that $\chi(0)$ would be constant for all soft-matter systems. This assumption helped Phan *et al.* capture the molecular dynamics of many drugs, polymers, and alloys in the supercooled state [77,79,127–129]. From there, we can expect that $\chi(0) = 6\times10^{-4}$ K^{-1} still works effectively for bcc Fe.

To reinforce our arguments, we compare Eq. (27) with

$$\chi(P,T) = \frac{\pi}{6}\sigma^3\rho(P,T)\alpha(P,T), \tag{28}$$

where the product of ρ and α is taken from the AIMD simulations of Bouchet *et al.* [54]. This comparison is detailed

in Fig. 3. Fundamentally, χ is barely affected by finite-temperature effects. Eq. (28) shows that χ climbs very slowly from 1.18×10^{-5} to 1.20×10^{-5} K^{-1} when bcc Fe is isobarically heated from 4983 to 6681 K at 360 GPa. That means we can ignore the thermal variation of χ in ECNLE approximations.

Another noteworthy feature is that AIMD outputs are only one-third of ECNLE counterparts at the IC center. Why does this discrepancy occur? We believe that this is due to the suppression of superionicity by the small cell sizes used by Bouchet *et al.* [54]. Bouchet *et al.* [54] simulated the bcc structure via a small supercell (128 atoms) with volume/shape restrictions. Their approach caused superionic excitations to be entirely suppressed, thereby underestimating the coefficient χ. As presented in Appendix C, there is a dramatic increase in χ after switching from nonsuperionic to superionic regimes. By considering the AIMD density-temperature profile of typical Fe-based crystals [39,130–132], we find out that χ often triples because of intrinsic superionicity. Interestingly, it is possible to draw the same conclusion from available experimental data for the thermal expansion of soft-matter systems in glassy and supercooled states [133]. The listed evidence corroborates the reliability of Eq. (27)—the last puzzle piece to complete Phan's mapping.

III. RESULTS AND DISCUSSION

A. Rheological properties

Figure 4 depicts how the mean square displacement of bcc Fe changes over time at $P = 360$ GPa. In general, $\langle r^2 \rangle$ grows linearly with t at an arbitrarily given temperature between 6000 and 7000 K. This tendency is in stark contrast to the case of hcp Fe, where $\langle r^2 \rangle$ is almost independent of t [59]. More intuitively speaking, in the hcp phase, Fe atoms primarily vibrate around their equilibrium positions. On the other hand, in the bcc phase, Fe atoms become more diffusive than usual. Hence, whereas hcp Fe acts like an ordinary solid, bcc Fe behaves like an exceptional liquid. This perspective is further clarified by analyzing the radial distribution function in Appendix D.

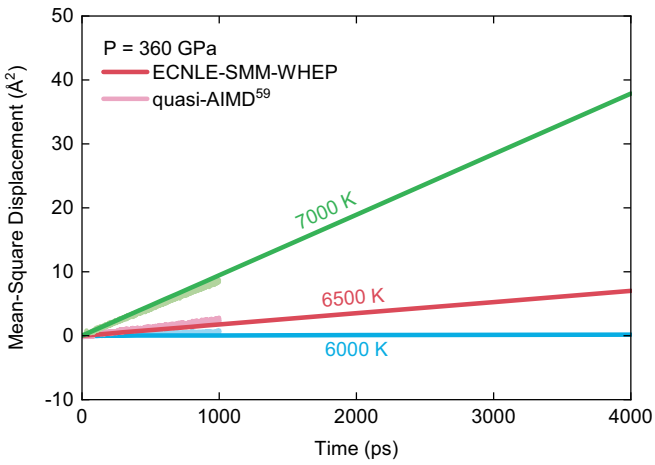

FIG. 4. The influence of temperature on the evolution of the mean-square displacement of Fe atoms in the bcc lattice at 360 GPa.

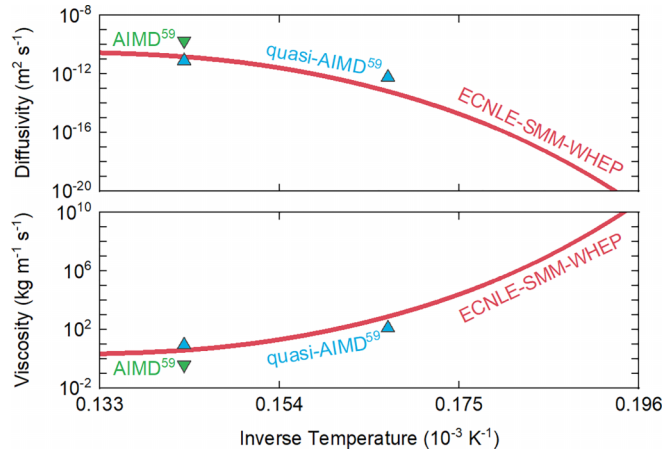

FIG. 5. Our theoretical predictions of the rheology of bcc Fe at the IC center. AIMD and quasi-AIMD data points [59] are also plotted to verify the reliability of the ECNLE-SMM-WHEP model.

It should be noted that tracing the evolution of $\langle r^2 \rangle$ in the bcc structure is a thorny issue in molecular dynamics computations. Take $T = 7000$ K as an example. The mean square displacement does not converge until the number of atoms reaches 128 000 [41]. Furthermore, if the simulation time is shorter than 10 ps, the signatures of superionic diffusion cannot be detected [59]. These stringent criteria cause the cost of establishing the $\langle r^2 \rangle$-t relationship to be prohibitively expensive.

Fortunately, the predicament we face here can be significantly improved by the ECNLE-SMM-WHEP. This combined theoretical approach helps accelerate computational processes dramatically while preserving the necessitated accuracy. Namely, it only takes us a few dozen minutes to finish ECNLE-SMM-WHEP calculations on our laptops. Besides, our numerical outcomes are in good accordance with the computational results of Belonoshko's group [59]. Recall that Belonoshko *et al.* used up to 2 048 000 atoms to simulate bcc Fe from 0 to 1000 ps with the aid of cutting-edge supercomputers [59]. With such treatment, the quality of their quasi-AIMD outputs was strictly ensured since unexpected finite-size and finite-time effects were safely eliminated [59].

Having determined the time variation of the mean square displacement, we can effortlessly investigate the rheological features of bcc Fe via Eq. (14), (15), and (18). Figure 5 illustrates how the diffusivity and the viscosity depend on the inverse temperature at Earth's center. Generally, while D decreases sharply during isobaric cooling, η increases considerably during the same process. If we raise T^{-1} from 0.133×10^{-3} to 0.196×10^{-3} K^{-1} at $P = 360$ GPa, D and η will vary by about ten orders of magnitude. Our observed trends align with the AIMD and quasi-AIMD data given by Belonoshko and coworkers [59]. The slight difference between the ECNLE-SMM-WHEP and the AIMD at $T = 7000$ K may stem from the finite-size problem. Admittedly, the capability of current supercomputers is insufficient to carry out AIMD simulations with more than 2000 Fe atoms [39,41,52,59,60]. This technical limitation may lead to an error in computing D and η. More attempts are needed to obtain a fully converged AIMD picture of bcc Fe under deep-Earth conditions.

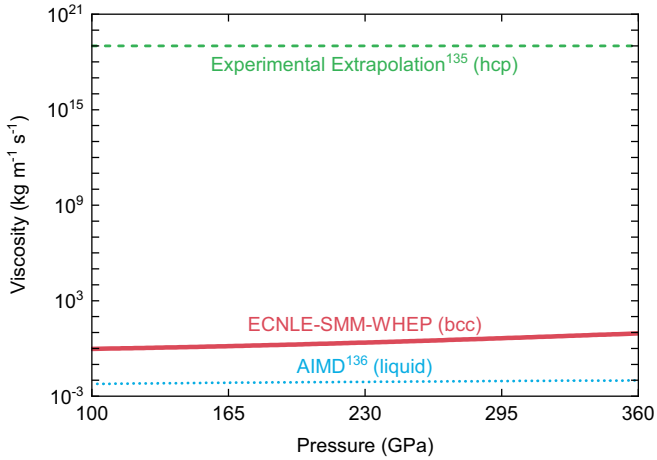

FIG. 6. The viscosity of Fe along the solid-liquid coexistence line gained from ECNLE-SMM-WHEP calculations, AIMD simulations [136], and uniaxial deformation experiments [135].

A vital point to highlight is that the temperature dependence of D and η does not obey the classical Arrhenius law [63]. Near T^*, a strong nonlinearity is recorded in the logarithm plot of these rheological quantities. So, what is the root of the non-Arrhenius behaviors of bcc Fe? The answer lies in its cooperative dynamics. Indeed, the collective barrier F_E grows at breakneck speed with reducing T [71–74]. This phenomenon makes the structural relaxation switch from the Arrhenius regime to the super-Arrhenius one when bcc Fe shrinks along isobars. In addition, according to Stokes [92] and Einstein [93], we have $\eta \propto D^{-1} \propto \tau_\alpha$. Thus it is understandable why the famed Arrhenius ansatz [63] is invalid in the present circumstance. The breakdown of the Arrhenius model reaffirms that there is a close analogy between supercooled and superionic materials. To be more specific, bcc Fe is closely analogous to an intermediate glass-forming liquid with a fragility index m^* of 89.47 at the IC center ($m^* = [\partial(\log_{10}\tau_\alpha)/\partial(T^*/T)]_{T=T*}$ [134]). Our theoretical findings concur with previous phenomenological and computational results [61,62,65,66].

Figure 6 shows how the viscosity of bcc Fe changes along the melting curve, which is one of the most critical paths to exploring Earth's interior [31–34]. Overall, our considered system is more and more viscous thanks to the positive contribution of hydrostatic pressures. When P goes up from 100 to 360 GPa, η climbs by a factor of 9.46 from 0.93 to 8.80 kg m^{-1} s^{-1}. Surprisingly, it is unlikely to find such low values in hcp models, even though both bcc Fe and hcp Fe exist within the crystalline state. By conducting uniaxial deformation experiments with D111-type and D-DIA apparatuses, Nishihara *et al.* [135] indicated that the hcp viscosity in the IC environment would be higher than 10^{19} kg m^{-1} s^{-1}, far beyond our predictions of the bcc phase in the same thermodynamic condition. Otherwise, by running AIMD computations in the projected-augmented-wave formalism, Li *et al.* [136] demonstrated that the viscosity of liquid Fe would range between 0.006 and 0.01 kg m^{-1} s^{-1} along the melting boundary. These AIMD outputs [136] are only a few hundred times lower than our ECNLE-SMM-WHEP outcomes in spite of the essential difference between liquid and solid structures. The above events suggest that the appearance of bcc Fe may be a key to solving a great puzzle about IC anelasticity [59], which has challenged our understanding of mineral physics for decades.

B. Mechanical properties

Figure 7 shows the shear modulus of Fe as a function of temperature at 360 GPa. In the hcp phase, a pronounced drop in G is recorded during isobaric heating. Notwithstanding, mineral-physics results [137–139] remain appreciably larger than seismic ones [140–142]. To bridge the gap, Martorell *et al.* [138] took into account premelting effects. This treatment generated a strong nonlinearity in the G-T profile at $T \geqslant$ 7000 K. Accordingly, G plunged to 180 GPa just before melting [138], in line with the preliminary reference Earth model (PREM) of Dziewonski and Anderson [140] ($G = 176$ GPa). Unfortunately, the above agreement seems to be an accident. Martorell *et al.* [138] only ran AIMD codes with a diminutive supercell containing 64 atoms. This figure is insufficient to avoid finite-size issues. Indeed, Li and Scandolo [139] developed a machine-learning interatomic potential for hcp Fe to reduce computational expenses while retaining AIMD accuracies. When the number of atoms increased to 1440, the nonlinear shear weakening was no longer observed in their MLMD simulations [139]. As an inevitable consequence, the profound contradiction between PREM and AIMD returned. This event highlights the enormous difficulties of interpreting seismic observations via the elastic features of the hcp structure.

Remarkably, everything would become much easier to solve if the IC is partially composed of bcc Fe. Our conclusion relies on the following two reasons. First, the ECNLE-SMM-WHEP theory reveals that the bcc structure is significantly softer than its hcp counterpart due to the superionic diffusion.

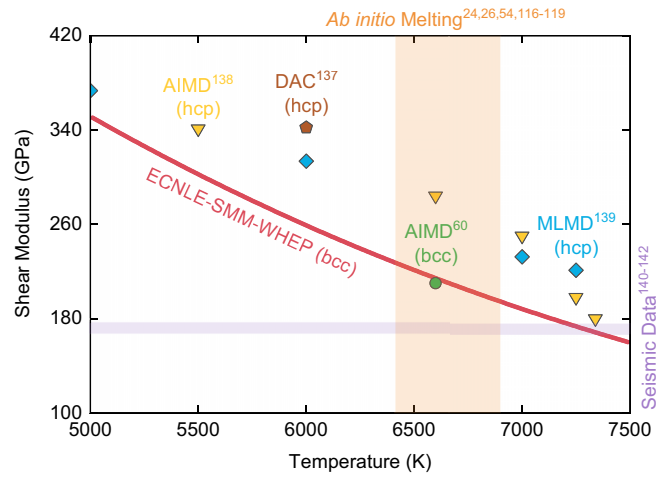

FIG. 7. ECNLE-SMM-WHEP, DAC [137], AIMD [60,138], and MLMD [139] estimations for the thermal variation of the shear modulus of Fe at 360 GPa. The orange-shaded area represents *ab initio* outputs for the melting point of Fe [24,26,54,116–119], while the purple-shaded one describes seismic results for the rigidity of the IC [140–142].

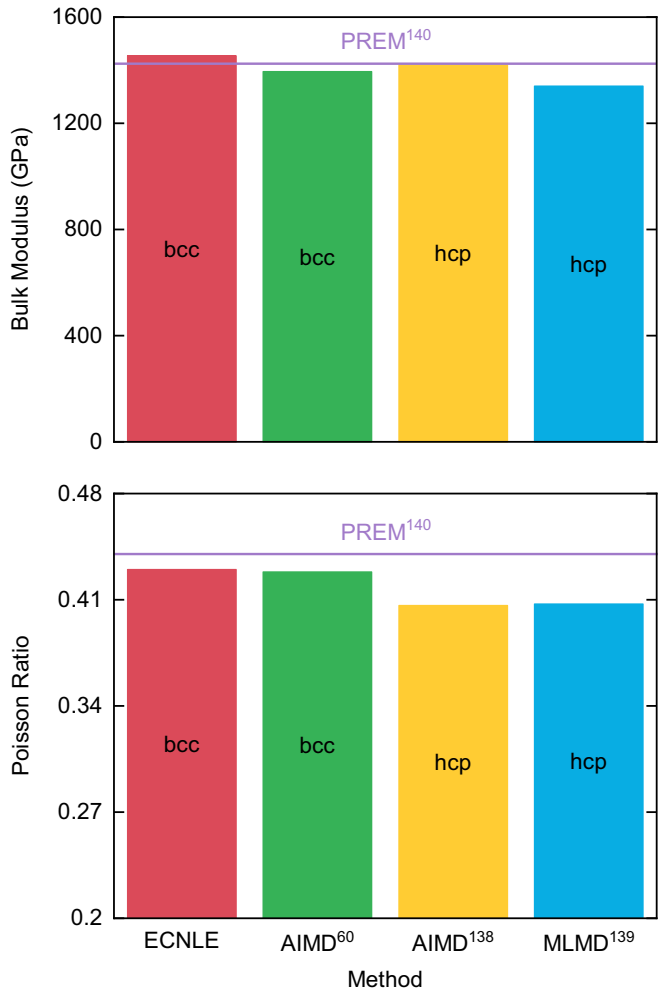

FIG. 8. The bulk modulus and the Poisson ratio of Fe derived from ECNLE-SMM-WHEP, AIMD [60,138], and MLMD [139] methods at 6600 K and 360 GPa. PREM data [140] for the IC are also added for comparison.

At the SMM-WHEP melting point, we acquire $G = 208$ GPa, about 27% lower than the AIMD data collected by Martorell and colleagues [138]. This finding is actively bolstered by the robust computations of Belonoshko *et al.* [60], who studied the unique mechanical responses of the bcc phase via the largest supercell ever designed for AIMD (2000 atoms). Second, in contrast to the case of hcp Fe, the shear softening in bcc Fe does not require unrealistic thermal conditions. To recreate the PREM rigidity [140], Martorell *et al.* [138] had to heat their samples to 7350 K, which fell entirely outside the *ab initio* melting region [24,26,54,116–119]. Meanwhile, our theoretical melting temperature is only about 6681 K, which is very suitable for modeling the IC interior [143–145].

Figure 8 shows the bulk modulus B and the Poisson ratio ν of Fe at 6600 K and 360 GPa. Theoretically, these elastic quantities are defined by [146]

$$B = \frac{\Phi}{\left(\frac{\partial \Phi}{\partial P}\right)_T}, \qquad \nu = \frac{3B - 2G}{2(3B + G)}. \tag{29}$$

Solving Eq. (29) by ECNLE-SMM-WHEP techniques brings us $B = 1454$ GPa and $\nu = 0.43$, nearly identical to PREM values [140] ($B = 1425$ GPa and $\nu = 0.44$). Excitingly, our numerical analyses for B are in consonance with prior atomistic simulations [60,138,139] regardless of using hcp or bcc structures. The maximum deviation between ECNLE-SMM-WHEP, AIMD [60,138], and MLMD [139] approaches is merely 9 %. This number implies that the strangely high Poisson ratio of the IC does not originate from its bulk modulus. Instead, the low rigidity is the root of the problem. Our discoveries are fervently supported by the large-scale *ab initio* calculations of Belonoshko's group [60].

Notably, despite achieving certain successes, our combined theory is temporarily not capable of describing the seismic anisotropy of the IC. In principle, dealing with anisotropic conundrums necessitates intimate knowledge of the elastic constants C_{ij} of single crystals [19,60,147]. Meanwhile, with the current level, the ECNLE-SMM-WHEP can only provide information about the elastic moduli of polycrystals. If we have C_{ij}, we can effortlessly infer G and B from the Voigt [148], Reuss [149], or Voigt-Reuss-Hill [150] approximations. However, the story becomes much more complicated when approaching from the inverse direction. As far as we know, there is no way to convert G and B to C_{ij}. Rebuilding the ECNLE reference system from nonspherical particles may be a viable strategy for circumventing these limitations. Hence, we believe the IC anisotropy deserves consideration in a separate ECNLE-SMM-WHEP study.

C. Geophysical implications

To illustrate the applicability of the ECNLE-SMM-WHEP scheme to Earth and planetary sciences, we revisit the long-standing controversy about the IC shear-wave attenuation [151]. Seismologically, the IC is the most attenuative part of our home planet, and its inverse quality factor Q_μ^{-1} is often measured via normal-mode or body-wave techniques. Whereas normal-mode measurements give $Q_\mu^{-1} = 0.0091$–0.0118 [152–155], body-wave experiments yield $Q_\mu^{-1} = 0.0032$–0.0083 [156–158]. Although seismic data exhibit a wide variation, none match the energy dissipation in hcp Fe. The inverse quality factor of the hcp structure is on the level of 10^{-4}–10^{-5} [53], far below normal-model and body-wave benchmarks [152–158]. The situation becomes even more alarming with the emergence of coda-correlation studies on the IC, where Q_μ^{-1} has to escalate to 0.0476 to reproduce synthetic waveforms [159].

The past forty years saw tireless attempts to gain a unified picture of IC anelasticity. Singh *et al.* [53] treated the IC as a two-phase composite consisting of a hcp Fe matrix and a liquid Fe filler. This idea allowed them to explain seismic observations quantitatively. Yet, Sumita *et al.* [160] demonstrated that liquid Fe would be expelled from the IC because of viscous compaction or convective instability. Recently, Belonoshko *et al.* [59] proposed that the IC would be principally made of bcc Fe rather than hcp Fe. This perspective enabled them to handle the IC attenuation without liquid inclusion. Nonetheless, the dominance of bcc Fe stays unconfirmed. Additionally, Xian *et al.* [161] were concerned that the bcc model

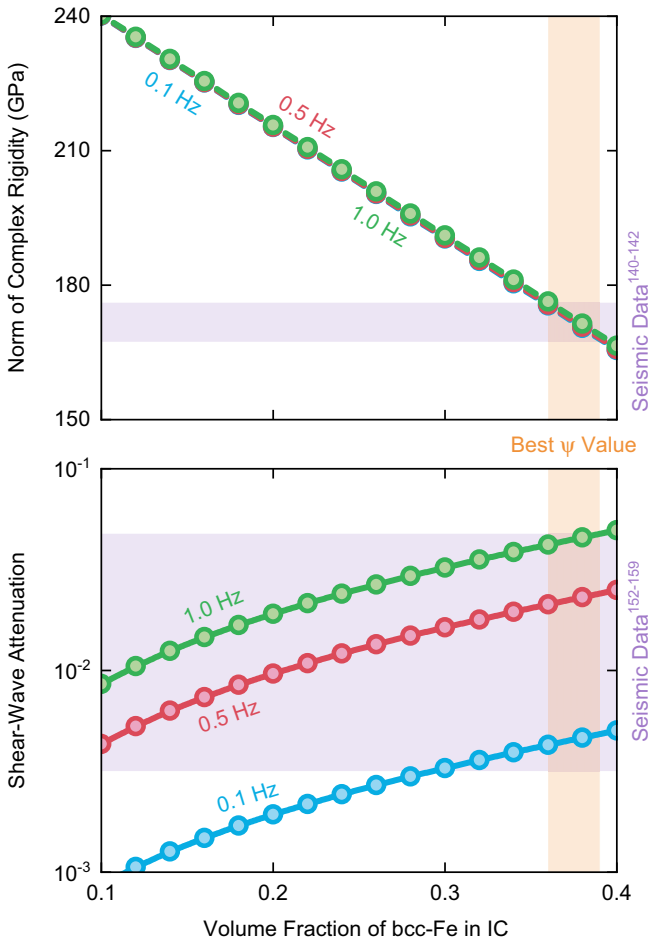

FIG. 9. The IC rigidity and the IC attenuation acquired from ECNLE-SMM-WHEP calculations (solid lines with filled circles) and seismic measurements [140–142,152–159] (purple-shaded regions). Orange-shaded areas are where theoretical predictions coincide with experimental observations.

of Belonoshko *et al.* [59] would cause a contradiction between the IC viscosity and the IC rigidity at seismic frequencies.

Herein, inspired by the latest publication of Zhang *et al.* [35], we describe the IC as a special combination of hcp and bcc phases. Mineralogically, this mixture can be formed thanks to the two-step nucleation of Fe [43] or the presence of bcc stabilizers S, Si, and Ni in the IC environment [46–48]. Seismologically, the hcp-bcc coexistence can be explored by scrutinizing the structural complexity at the OC-IC interface [35]. Therefore our assumption is acceptable. To quickly estimate the inverse quality factor of the IC, we adopt the effective medium theory of Singh *et al.* [53]. Specifically, the complex shear modulus μ is written by

$$\mu = \mu_0 - \frac{2}{15}\mu_0\psi\left\{\frac{8}{3}\left(\frac{\lambda_0+2\mu_0}{\lambda_0+\mu_0}\right)\left(\frac{1+2\pi i f\tau}{1+2\pi i f\Upsilon\tau}\right) + 16\left(\frac{\lambda_0+2\mu_0}{3\lambda_0+4\mu_0}\right)\left[1+\frac{8if\eta a}{\mu_0 c}\left(\frac{\lambda_0+2\mu_0}{3\lambda_0+4\mu_0}\right)\right]^{-1}\right\},$$
$$\Upsilon = 1+\frac{a}{\pi c}\frac{\kappa_0}{\mu_0}\left(\frac{\lambda_0+2\mu_0}{\lambda_0+\mu_0}\right),\quad \tau = \frac{10^{-12}}{\psi^2}\frac{\psi_m\eta}{K_m B}. \tag{30}$$

TABLE I. Inputs to our IC model [Eqs. (30) and (31)].

Symbol	Definition	Value	Reference
f	Frequency of seismic wave	0.1–1 Hz	[157–159]
μ_0	Shear modulus of hcp matrix	265 GPa	[139]
κ_0	Bulk modulus of hcp matrix	1340 GPa	[139]
λ_0	Lame constant of hcp matrix	1163 GPa	[139]
ψ_m	Porosity of hcp matrix	0.4	[162]
K_m	Permeability of hcp matrix	10^{-18} m^2	[53]
ψ	Volume fraction of bcc filler	0.1–0.4	This work
a/c	Aspect ratio of bcc filler	1	This work
η	Viscosity of bcc filler	8.8 Pa s	This work
B	Bulk modulus of bcc filler	1454 GPa	This work

Details about Eq. (30) are supplied in Table I [53,139,157–159,162]. From there, it is feasible to determine Q_μ^{-1} by

$$Q_\mu^{-1} = \frac{\mathrm{Im}(\mu)}{\mathrm{Re}(\mu)}. \tag{31}$$

Figure 9 depicts the IC rigidity and the IC attenuation as a function of the volume fraction of bcc Fe at different frequencies. Similar to recent seismic investigations into the IC, we focus on a frequency range from 0.1 to 1 Hz [157–159]. Generally, whereas $|\mu|$ is almost unaffected by f, Q_μ^{-1} is extremely sensitive to the period of seismic signals. This sensitivity may be the origin of the discrepancy between normal-mode [152–155], body-wave [156–158], and coda-correlation [159] measurements on Q_μ^{-1}. Another possible cause is the depth dependence of Q_μ^{-1} [151]. Normal modes are primarily employed to probe the IC top. Meanwhile, body and coda waves are mainly applied to penetrate deep into the IC.

Remarkably, with $\psi = 0.36$–0.39, we can simultaneously answer why the IC is so soft and attenuative. Our ECNLE-SMM-WHEP analyses are congruent with the DAC experiments of Ituka *et al.* [48], where the bcc structure often accounts for 26%, 36%, or 42% of the volume of Fe-Ni-Si alloys after decomposition. Moreover, the viscosity-rigidity paradox raised by Xian's group [161] is resolved. In our physical picture, the low viscosity of bcc Fe does not make the IC shear resistance unrealistic. Conversely, this unique property is highly advantageous for decoding seismic results as long as bcc Fe and hcp Fe are mixed with appropriate ratios. A better description of the IC can be reached if the influence of light elements is explicitly taken into account. Our findings would open a promising avenue for unraveling the mystery of planetary interiors.

IV. CONCLUSION

We have merged the ECNLE with the SMM-WHEP to generate a useful theoretical tool for capturing the liquidlike behaviors of bcc Fe under extreme conditions. This tool has helped us compute the rheological and mechanical properties of the bcc structure at breakneck speed. A quantitative consistency between our calculations and simulations has been achieved. Furthermore, a reasonable explanation for the IC viscoelasticity has been provided. These encouraging

outcomes have shown the effectiveness of the ECNLE-SMM-WHEP method in geophysical applications. To facilitate subsequent research projects on the IC, we have expressed all physical quantities in explicit analytical forms. All crucial data have also been carefully systematized in appendices. We are eager to see new advances in this challenging field in the foreseeable future.

ACKNOWLEDGMENTS

We thank anonymous referees for their valuable comments and suggestions.

APPENDIX A: ECNLE GENERAL OUTPUTS

Our hard-sphere calculations are shown in Table II.

APPENDIX B: SMM EQUATION OF STATE

In this Appendix, we briefly introduce how to determine the EoS parameters of bcc Fe at room temperature $T_r = 300$ K.

First of all, since T_r is far below T^*, we can view bcc Fe as an ordinary solid at T_r. Accordingly, in the thermodynamic equilibrium state, the displacement of Fe atoms, characterized by the n-th order moment $\langle u^n \rangle$, has to satisfy [80]

$$k\langle u\rangle + \gamma\langle u^3\rangle - p = 0. \tag{B1}$$

Here, k is a quasiharmonic coefficient, γ is an anharmonic coefficient, and p is a supplemental force. Applying the Leibfried-Ludwig expansion [163] to the quasi *ab initio* potential energy E of Ye *et al.* [164] brings us

$$k = \left(\frac{\partial^2 E}{\partial u_\delta^2}\right)_{eq}, \quad \gamma = \frac{1}{6}\left(\frac{\partial^4 E}{\partial u_\delta^4}\right)_{eq} + \left(\frac{\partial^4 E}{\partial u_\delta^2 \partial u_\zeta^2}\right)_{eq}, \tag{B2}$$

TABLE II. The mechanical and rheological features of the EC-NLE reference system at different packing fractions

Φ	$\frac{G\sigma^3}{k_BT}$	$\log_{10}\tau_\alpha$ (s)	$\log_{10}\frac{D}{\sigma^2}$ (s^{-1})	$\log_{10}\frac{\eta\sigma^3}{k_BT}$ (s)
0.44	10.4505	−11.2298	8.3004	−9.0983
0.45	11.7861	−11.1905	8.5749	−9.3729
0.46	13.2955	−11.1377	8.6865	−9.4844
0.47	15.0019	−11.0789	8.7363	−9.5342
0.48	16.9323	−11.0149	8.7524	−9.5504
0.49	19.1173	−10.9450	8.7460	−9.5439
0.50	21.5924	−10.8665	8.7207	−9.5187
0.51	24.3981	−10.7733	8.6747	−9.4727
0.52	27.5815	−10.6532	8.5985	−9.3964
0.53	31.1969	−10.4796	8.4678	−9.2658
0.54	35.3073	−10.2043	8.2359	−9.0339
0.55	39.9856	−9.7610	7.8376	−8.6356
0.56	45.3172	−9.0932	7.2170	−8.0150
0.57	51.4013	−8.1497	6.3223	−7.1202
0.58	58.3546	−6.8333	5.0552	−5.8531
0.59	66.3136	−4.9817	3.2515	−4.0494
0.60	75.4395	−2.2904	0.6051	−1.4031
0.61	85.9226	1.5582	−3.2029	2.4050
0.62	97.9887	7.0477	−8.6562	7.8583

TABLE III. The influence of hydrostatic compression on the cube root of the normalized atomic volume provided by room-temperature SMM calculations for bcc Fe.

P (GPa)	ξ	P (GPa)	ξ
0	1.0000	1600	0.7279
10	0.9862	1700	0.7230
20	0.9746	1800	0.7184
30	0.9647	1900	0.7140
40	0.9560	2000	0.7099
50	0.9482	2100	0.7059
60	0.9411	2200	0.7021
70	0.9346	2300	0.6985
80	0.9287	2400	0.6950
90	0.9231	2500	0.6917
100	0.9180	2600	0.6885
200	0.8793	2700	0.6854
300	0.8532	2800	0.6824
400	0.8334	2900	0.6795
500	0.8175	3000	0.6768
600	0.8041	3100	0.6741
700	0.7925	3200	0.6715
800	0.7824	3300	0.6689
900	0.7733	3400	0.6665
1000	0.7651	3500	0.6641
1100	0.7577	3600	0.6618
1200	0.7508	3700	0.6595
1300	0.7445	3800	0.6573
1400	0.7386	3900	0.6552
1500	0.7330	4000	0.6531

where δ and ζ are the Cartesian indexes ($\delta \neq \zeta = x, y, z$). The explicit form of k and γ can be obtained by following the instructions in Supplemental Material of Refs. [99,107].

Next, we utilize the SMM to solve the mentioned force-balance criterion. This statistical method allows us to connect all of the moments of the studied system via the quantum density matrix [105,106]. Namely, $\langle u^3 \rangle$ is represented via $\langle u \rangle$ as follows [80]:

$$\langle u^3\rangle = \langle u\rangle^3 + 3\theta\langle u\rangle\frac{\partial\langle u\rangle}{\partial p} + \theta^2\frac{\partial^2\langle u\rangle}{\partial p^2} + \frac{\theta}{k}(X-1)\langle u\rangle,$$
$$\theta = k_BT, \quad X = \frac{\hbar\omega}{2\theta}\coth\frac{\hbar\omega}{2\theta}, \quad \omega = \sqrt{\frac{k}{m}}, \tag{B3}$$

where $\hbar$ is the reduced Planck constant and m is the atomic mass. Inserting Eq. (B3) into Eq. (B1) leads to

$$\gamma\theta^2\frac{\partial^2\langle u\rangle}{\partial p^2} + 3\gamma\theta\langle u\rangle\frac{\partial\langle u\rangle}{\partial p} + \gamma\langle u\rangle^3 + k\langle u\rangle + \frac{\gamma\theta}{k}(X-1)\langle u\rangle - p = 0. \tag{B4}$$

Conspicuously, Eq. (B4) only contains a single variable $\langle u \rangle$, so we can readily handle it via the Tang iterative technique [165]. When p goes to zero, we have [80]

$$\langle u\rangle = \sqrt{\frac{2\gamma\theta^2}{3k^3}}A, \tag{B5}$$

where A is a dimensionless quantity [166–168]. On that basis, the cube root of the normalized atomic volume ξ is given by

$$\xi = \frac{d(P,0) + \langle u\rangle(P,T_r)}{d(0,0) + \langle u\rangle(0,T_r)}, \tag{B6}$$

where d is the nearest neighbor distance.

Finally, our numerical results for ξ are listed in Table III. Fitting them with the Vinet EoS [101] yields $B_0 = 198.76$ GPa and $B_0' = 5.05$. These parameters entirely concur with the AIMD data of Belonoshko *et al.* [130] ($B_0 = 198.07$ GPa, $B_0' = 5.426$) and Bouchet *et al.* [54] ($B_0 = 199.520$ GPa, $B_0' = 5.070$). Thus they can serve as high-quality inputs to the WHEP program to predict the melting characteristics of bcc Fe in planetary cores.

APPENDIX C: SUPERIONIC DIFFUSION VERSUS THERMAL EXPANSION

To elucidate the impact of superionic diffusion on thermal expansion, we employ

$$\frac{\chi(P,T>T^*)}{\chi(P,T<T^*)} = \frac{\left(\frac{\partial\rho}{\partial T}\right)_{P,T>T^*}}{\left(\frac{\partial\rho}{\partial T}\right)_{P,T<T^*}}, \tag{C1}$$

where the right-hand side is computed by fitting density-temperature data with linear functions. Figure 10 displays our analyses based on available AIMD information about bcc Fe [39,130], hcp FeC [131], and hcp FeH [132] at 360 GPa. It is easy to see that the slope of density-temperature profiles changes abruptly at T^* [Fig. 10(a)]. Although the tested systems have different structures and components, their density variations obey the same rule. After the superionic transition occurs, the coefficient χ increases about threefold irrespective of whether bcc or hcp lattices are studied [Fig. 10(b)]. This phenomenon is strikingly similar to what happens in glass formers. As proven by Lunkenheimer *et al.* [133], the volumetric expansivity of soft materials always grows by a factor of 3 after transforming from glassy to supercooled states. Hence, it is plausible to model the dilation of superionic bcc Fe via Eq. (27).

APPENDIX D: RADIAL DISTRIBUTION FUNCTION

Figure 11 presents the radial distribution function of bcc Fe at 360 GPa. Overall, we can quantitatively understand the spatial arrangement of Fe atoms via the Percus-Yevick theory [81]—a ubiquitous approximation in the soft-matter community [71–79]. The proof is that Percus-Yevick and AIMD profiles are pretty much the same. Our Percus-Yevick analyses reveal that $g(r)$ reaches the first minimum at $r_{\min} = 1.38\sigma$ and the first maximum at $r_{\max} = 2.01\sigma$, consistent with $r_{\min} = 1.40\sigma$ and $r_{\max} = 1.90\sigma$ predicted by the AIMD simulations of Belonoshko *et al.* [59]. Additionally, the effective coordination number can be calculated by the Percus-Yevick integral as $N = 4\pi\rho\int_0^{r_{\min}} r^2 g(r)dr = 12$, congruent with $N = 11$ inferred from the AIMD method [52]. It is conspicuous that the obtained numbers are markedly higher than previously thought ($N = 8$ [30]). The reason is that the drastic thermal motion of Fe atoms in the bcc lattice can result in the overlap between the first and second neighboring shells at elevated

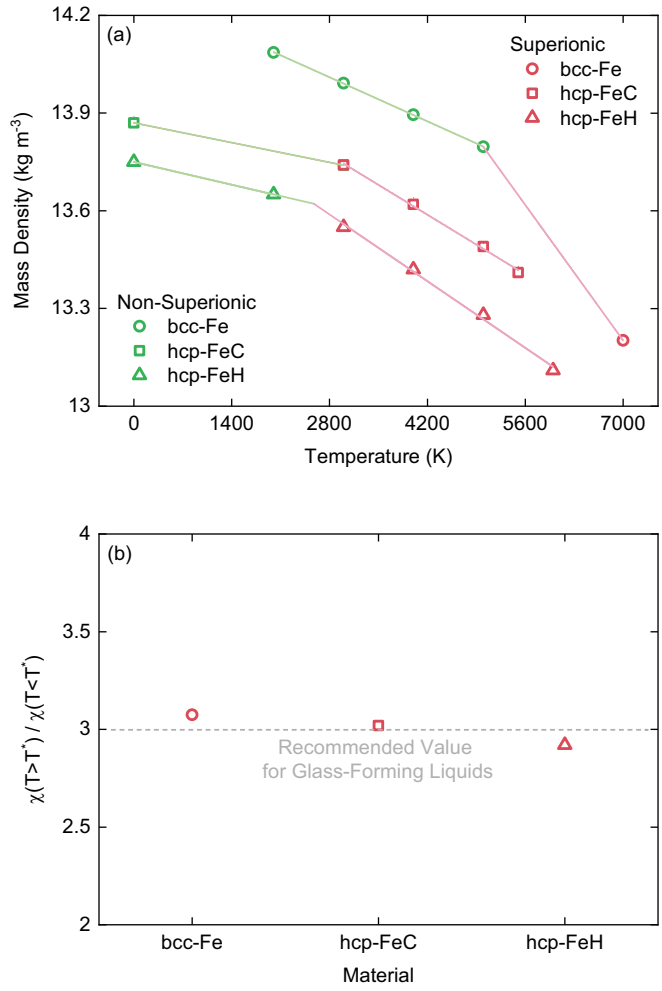

FIG. 10. (a) The density-temperature profile of bcc Fe, hcp FeC, and hcp FeH given by prior AIMD simulations [39,130–132] (open symbols) and our linear fits (solid lines) at 360 GPa. (b) Our estimations for the χ enhancement of bcc Fe, hcp FeC, and hcp FeH due to superionic effects (open symbols). The latest result of Lunkenheimer *et al.* [133] is also included to highlight the resemblance between superionic crystals and glass formers (dashed line).

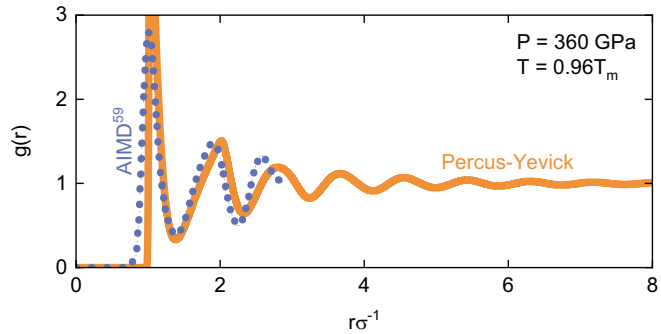

FIG. 11. Our Percus-Yevick calculations versus the large-scale AIMD computations of Belonoshko *et al.* [59] for the radial distribution function of bcc Fe.

temperatures [52]. Remark that no adjustable parameters are needed to achieve the consensus between Percus-Yevick and AIMD calculations. That means bcc Fe is indeed equivalent to a glass-forming liquid.

[1] I. Lehmann, P′, Publ. Bur. Cent. Seismol. Int. Sér. A Trav. Sci. **14**, 87 (1936).

[2] H. Tkalčić, Complex inner core of the Earth: The last frontier of global seismology, Rev. Geophys. **53**, 59 (2015).

[3] G. Pang, K. D. Koper, S. M. Wu, W. Wang, M. Lasbleis, and G. Euler, Enhanced inner core fine-scale heterogeneity towards Earth's centre, Nature (London) **620**, 570 (2023).

[4] R. Deguen, Structure and dynamics of Earth's inner core, Earth Planet. Sci. Lett. **333-334**, 211 (2012).

[5] B. J. Foley and P. E. Driscoll, Whole planet coupling between climate, mantle, and core: Implications for rocky planet evolution, Geochem. Geophys. Geosyst. **17**, 1885 (2016).

[6] C. A. Jones, *Treatise on Geophysics*, 2nd ed. (Elsevier, Amsterdam, 2015), Vol. 8, p.115.

[7] M. Landeau, A. Fournier, H. C. Nataf, D. Cebron, and N. Schaeffer, Sustaining Earth's magnetic dynamo, Nat. Rev. Earth Environ. **3**, 255 (2022).

[8] G. Schubert, Numerical models of mantle convection, Annu. Rev. Fluid Mech. **24**, 359 (1992).

[9] D. Bercovici, The generation of plate tectonics from mantle convection, Earth Planet. Sci. Lett. **205**, 107 (2003).

[10] C. P. Conrad, T. A. Bianco, E. I. Smith, and P. Wessel, Patterns of intraplate volcanism controlled by asthenospheric shear, Nat. Geosci. **4**, 317 (2011).

[11] R. Moucha and A. M. Forte, Changes in African topography driven by mantle convection, Nat. Geosci. **4**, 707 (2011).

[12] C. Prescher, L. Dubrovinsky, E. Bykova, I. Kupenko, K. Glazyrin, A. Kantor, C. McCammon, M. Mookherjee, Y. Nakajima, N. Miyajima, R. Sinmyo, V. Cerantola, N. Dubrovinskaia, V. Prakapenka, R. Rüffer, A. Chumakov, and M. Hanfland, High Poisson's ratio of Earth's inner core explained by carbon alloying, Nat. Geosci. **8**, 220 (2015).

[13] S. Boccato, R. Torchio, I. Kantor, G. Morard, S. Anzellini, R. Giampaoli, R. Briggs, A. Smareglia, T. Irifune, and S. Pascarelli, The melting curve of nickel up to 100 GPa explored by XAS, J. Geophys. Res.: Solid Earth **122**, 9921 (2017).

[14] W. Liu, Y. Zhang, Q. Z. Yin, Y. Zhao, and Z. Zhang, Magnesium partitioning between silicate melt and liquid iron using first-principles molecular dynamics: Implications for the early thermal history of the Earth's core, Earth Planet. Sci. Lett. **531**, 115934 (2020).

[15] K. Hirose, B. Wood, and L. Vocadlo, Light elements in the Earth's core, Nat. Rev. Earth Environ. **2**, 645 (2021).

[16] W. Luo, B. Johansson, O. Eriksson, S. Arapan, P. Souvatzis, M. I. Katsnelson, and R. Ahuja, Dynamical stability of body center cubic iron at the Earth's core conditions, Proc. Natl. Acad. Sci. USA **107**, 9962 (2010).

[17] S. Ritterbex and T. Tsuchiya, Viscosity of hcp iron at Earth's inner core conditions from density functional theory, Sci. Rep. **10**, 6311 (2020).

[18] M. Mattesini, A. B. Belonoshko, E. Buforn, M. Ramirez, S. I. Simak, A. Udias, H. K. Mao, and R. Ahuja, Hemispherical anisotropic patterns of the Earth's inner core, Proc. Natl. Acad. Sci. USA **107**, 9507 (2010).

[19] A. Dewaele, B. Amadon, A. Bosak, V. Svitlyk, and F. Occelli, Synthesis of single crystals of ϵ-iron and direct measurements of its elastic constants, Phys. Rev. Lett. **131**, 034101 (2023).

[20] S. Tateno, K. Hirose, Y. Ohishi, and Y. Tatsumi, The structure of iron in Earth's inner core, Science **330**, 359 (2010).

[21] L. Stixrude, Structure of iron to 1 Gbar and 40 000 K, Phys. Rev. Lett. **108**, 055505 (2012).

[22] B. Romanowicz, A. Cao, B. Godwal, R. Wenk, S. Ventosa, and R. Jeanloz, Seismic anisotropy in the Earth's innermost inner core: Testing structural models against mineral physics predictions, Geophys. Res. Lett. **43**, 93 (2016).

[23] D. A. Frost, M. Lasbleis, B. Chandler, and B. Romanowicz, Dynamic history of the inner core constrained by seismic anisotropy, Nat. Geosci. **14**, 531 (2021).

[24] F. Gonzalez-Cataldo and B. Militzer, *Ab initio* determination of iron melting at terapascal pressures and Super-Earths core crystallization, Phys. Rev. Res. **5**, 033194 (2023).

[25] L. Vočadlo, J. Brodholt, D. Alfe, M. J. Gillan, and G. D. Price, *Ab initio* free energy calculations on the polymorphs of iron at core conditions, Phys. Earth Planet. Inter. **117**, 123 (2000).

[26] Y. Sun, M. I. Mendelev, F. Zhang, X. Liu, B. Da, C. Z. Wang, R. M. Wentzcovitch, and K. M. Ho, *Ab initio* melting temperatures of bcc and hcp iron under the Earth's inner core condition, Geophys. Res. Lett. **50**, e2022GL102447 (2023).

[27] C. J. Wu, L. X. Benedict, P. C. Myint, S. Hamel, C. J. Prisbrey, and J. R. Leek, Wide-ranged multiphase equation of state for iron and model variations addressing uncertainties in high-pressure melting, Phys. Rev. B **108**, 014102 (2023).

[28] I. A. Kruglov, A. V. Yanilkin, Y. Propad, A. B. Mazitov, P. Rachitskii, and A. R. Oganov, Crystal structure prediction at finite temperatures, npj Comput. Mater. **9**, 197 (2023).

[29] Y. Zhang, Y. Wang, Y. Huang, J. Wang, Z. Liang, L. Hao, Z. Gao, J. Li, Q. Wu, H. Zhang, Y. Liu, J. Sun, and J. F. Lin, Collective motion in hcp Fe at Earth's inner core conditions, Proc. Natl. Acad. Sci. USA **120**, e2309952120 (2023).

[30] Y. Ping, F. Coppari, D. G. Hicks, B. Yaakobi, D. E. Fratanduono, S. Hamel, J. H. Eggert, J. R. Rygg, R. F. Smith, D. C. Swift, D. G. Braun, T. R. Boehly, and G. W. Collins, Solid iron compressed up to 560 GPa, Phys. Rev. Lett. **111**, 065501 (2013).

[31] R. G. Kraus, R. J. Hemley, S. J. Ali, J. L. Belof, L. X. Benedict, J. Bernier, D. Braun, R. E. Cohen, G. W. Collins, F. Coppari, M. P. Desjarlais, D. Fratanduono, S. Hamel, A. Krygier, A. Lazicki, J. Mcnaney, M. Millot, P. C. Myint, M. G. Newman, J. R. Rygg *et al.*, Measuring the melting curve of iron at super-Earth core conditions, Science **375**, 202 (2022).

[32] R. Boehler, Temperatures in the Earth's core from melting-point measurements of iron at high static pressures, Nature (London) **363**, 534 (1993).

[33] S. Anzellini, A. Dewaele, M. Mezouar, P. Loubeyre, and G. Morard, Melting of iron at Earth's inner core boundary based on fast X-ray diffraction, Science **340**, 464 (2013).

[34] R. Sinmyo, K. Hirose, and Y. Ohishi, Melting curve of iron to 290 GPa determined in a resistance-heated diamond-anvil cell, Earth Planet. Sci. Lett. **510**, 45 (2019).

[35] B. Zhang, S. Ni, W. Wu, Z. Shen, W. Wang, D. Sun, and Z. Wu, Small-scale layered structures at the inner core boundary, Nat. Commun. **14**, 6362 (2023).

[36] T. Wang, X. Song, and H. H. Xia, Equatorial anisotropy in the inner part of Earth's inner core from autocorrelation of earthquake coda, Nat. Geosci. **8**, 224 (2015).

[37] M. Mattesini, A. B. Belonoshko, H. Tkalcic, E. Buforn, A. Udias, and R. Ahuja, Candy wrapper for the Earth's inner core, Sci. Rep. **3**, 2096 (2013).

[38] B. K. Godwal, F. Gonzalez-Cataldo, A. K. Verma, L. Stixrude, and R. Jeanloz, Stability of iron crystal structures at 0.3–1.5 TPa, Earth Planet. Sci. Lett. **409**, 299 (2015).

[39] A. B. Belonoshko, T. Lukinov, J. Fu, J. Zhao, S. Davis, and S. I. Simak, Stabilization of body-centred cubic iron under inner-core conditions, Nat. Geosci. **10**, 312 (2017).

[40] A. J. Schultz, S. G. Moustafa, and D. A. Kofke, No system-size anomalies in entropy of bcc iron at Earth's inner-core conditions, Sci. Rep. **8**, 7295 (2018).

[41] A. B. Belonoshko, J. Fu, and G. Smirnov, Free energies of iron phases at high pressure and temperature: Molecular dynamics study, Phys. Rev. B **104**, 104103 (2021).

[42] L. Huguet II, J. A. Van Orman, S. A. Hauck II, and M. A. Willard, Earth's inner core nucleation paradox, Earth Planet. Sci. Lett. **487**, 9 (2018).

[43] Y. Sun, F. Zhang, M. I. Mendelev, R. M. Wentzcovitch, and K. M. Ho, Two-step nucleation of the Earth's inner core, Proc. Natl. Acad. Sci. USA **119**, e2113059119 (2022).

[44] L. Vočadlo, D. Alfe, M. J. Gillan, I. G. Wood, J. P. Brodholt, and G. D. Price, Possible thermal and chemical stabilization of body-centred-cubic iron in the Earth's core, Nature (London) **424**, 536 (2003).

[45] N. A. Smirnov, *Ab initio* calculations of structural stability, thermodynamic and elastic properties of Ni, Pd, Rh, and Ir at high pressures, J. Appl. Phys. **134**, 025901 (2023).

[46] H. Ozawa, K. Hirose, T. Suzuki, Y. Ohishi, and N. Hirao, Decomposition of Fe_3S above 250 GPa, Geophys. Res. Lett. **40**, 4845 (2013).

[47] S. Tateno, Y. Kuwayama, K. Hirose, and Y. Ohishi, The structure of Fe–Si alloy in Earth's inner core, Earth Planet. Sci. Lett. **418**, 11 (2015).

[48] D. Ikuta, E. Ohtani, and N. Hirao, Two-phase mixture of iron–nickel–silicon alloys in the Earth's inner core, Commun. Earth Environ. **2**, 225 (2021).

[49] F. Zhang and A. R. Oganov, Iron silicides at pressures of the Earth's inner core, Geophys. Res. Lett. **37**, L02305 (2010).

[50] P. N. Gavryushkin, Z. I. Popov, K. D. Litasov, A. B. Belonoshko, and A. Gavryushkin, Stability of B2-type FeS at Earth's inner core pressures, Geophys. Res. Lett. **43**, 8435 (2016).

[51] Y. Sun, M. I. Mendelev, F. Zhang, X. Liu, B. Da, C. Z. Wang, R. M. Wentzcovitch, and K. M. Ho, Unveiling the effect of Ni on the formation and structure of Earth's inner core, Proc. Natl. Acad. Sci. USA **121**, e2316477121 (2024).

[52] A. B. Belonoshko and G. S. Smirnov, A comparison of experimental and *ab initio* structural data on Fe under extreme conditions, Metals **13**, 1096 (2023).

[53] S. C. Singh, M. A. J. Taylor, and J. P. Montagner, On the presence of liquid in Earth's inner core, Science **287**, 2471 (2000).

[54] J. Bouchet, S. Mazevet, G. Morard, F. Guyot, and R. Musella, *Ab initio* equation of state of iron up to 1500 GPa, Phys. Rev. B **87**, 094102 (2013).

[55] L. V. Pourovskii, J. Mravlje, M. Pozzo, and D. Alfe, Electronic correlations and transport in iron at Earth's core conditions, Nat. Commun. **11**, 4105 (2020).

[56] D. Gambino, M. A. Brannvall, A. Ehn, Y. Hedstrom, and B. Alling, Longitudinal spin fluctuations in bcc and liquid Fe at high temperature and pressure calculated with a supercell approach, Phys. Rev. B **102**, 014402 (2020).

[57] M. Ghosh, S. Zhang, L. Hu, and S. X. Hu, Cooperative diffusion in body-centered cubic iron in Earth and super-Earths' inner core conditions, J. Phys.: Condens. Matter **35**, 154002 (2023).

[58] M. Arale Brännvall, D. Gambino, R. Armiento, and B. Alling, Machine learning approach for longitudinal spin fluctuation effects in bcc Fe at T_c and under Earth-core conditions, Phys. Rev. B **105**, 144417 (2022).

[59] A. B. Belonoshko, J. Fu, T. Bryk, S. I. Simak, and M. Mattesini, Low viscosity of the Earth's inner core, Nat. Commun. **10**, 2483 (2019).

[60] A. B. Belonoshko, S. I. Simak, W. Olovsson, and O. Y. Vekilova, Elastic properties of body-centered cubic iron in Earth's inner core, Phys. Rev. B **105**, L180102 (2022).

[61] A. Gray-Weale and P. A. Madden, Dynamical arrest in superionic crystals and supercooled liquids, J. Phys. Chem. B **108**, 6624 (2004).

[62] A. Gray-Weale and P. A. Madden, The energy landscape of a fluorite-structured superionic conductor, J. Phys. Chem. B **108**, 6634 (2004).

[63] S. A. Arrhenius, Ìber die Dissociationswärme und den Einfluss der Temperatur auf den Dissociationsgrad der Elektrolyte, Z. Phys. Chem. **4U**, 96 (1889).

[64] G. Adam and J. H. Gibbs, On the temperature dependence of cooperative relaxation properties in glass-forming liquids, J. Chem. Phys. **43**, 139 (1965).

[65] H. Zhang, X. Wang, A. Chremos, and J. F. Douglas, Superionic UO_2: A model anharmonic crystalline material, J. Chem. Phys. **150**, 174506 (2019).

[66] H. Zhang, X. Wang, and J. F. Douglas, Localization model description of diffusion and structural relaxation in superionic crystalline UO_2, J. Chem. Phys. **151**, 071101 (2019).

[67] A. D. Phan, K. Wakabayashi, M. Paluchd, and V. D. Lam, Effects of cooling rate on structural relaxation in amorphous drugs: elastically collective nonlinear Langevin equation theory and machine learning study, RSC Adv. **9**, 40214 (2019).

[68] P. S. Ghosh, A. Arya, G. K. Dey, N. Kuganathan, and R. W. Grimes, A computational study on the superionic behaviour of ThO_2, Phys. Chem. Chem. Phys. **18**, 31494 (2016).

[69] C. Takoukam-Takoundjou, E. Bourasseau, and V. Lachet, Study of thermodynamic properties of $U_{1-y}Pu_yO_2$ MOX fuel using classical molecular Monte Carlo simulations, J. Nucl. Mater. **534**, 152125 (2020).

[70] P. C. M. Fossati, A. Chartier, and A. Boulle, Structural aspects of the superionic transition in AX_2 compounds with the fluorite structure, Front. Chem. **9**, 723507 (2021).

[71] S. Mirigian and K. S. Schweizer, Unified theory of activated relaxation in liquids over 14 decades in time, J. Phys. Chem. Lett. **4**, 3648 (2013).

[72] S. Mirigian and K. S. Schweizer, Elastically cooperative activated barrier hopping theory of relaxation in viscous fluids. I. General formulation and application to hard sphere fluids, J. Chem. Phys. **140**, 194506 (2014).

[73] S. Mirigian and K. S. Schweizer, Elastically cooperative activated barrier hopping theory of relaxation in viscous fluids. II. Thermal liquids, J. Chem. Phys. **140**, 194507 (2014).

[74] A. D. Phan, J. Knapik-Kowalczuk, M. Paluch, T. X. Hoang, and K. Wakabayashi, Theoretical model for the structural relaxation time in coamorphous drugs, Mol. Pharmaceutics **16**, 2992 (2019).

[75] A. D. Phan and K. S. Schweizer, Elastically collective nonlinear Langevin equation theory of glass-forming liquids: Transient localization, thermodynamic mapping, and cooperativity, J. Phys. Chem. B **122**, 8451 (2018).

[76] S. Mirigian and K. S. Schweizer, Dynamical theory of segmental relaxation and emergent elasticity in supercooled polymer melts, Macromolecules **48**, 1901 (2015).

[77] A. D. Phan, Determination of Young's modulus of active pharmaceutical ingredients by relaxation dynamics at elevated pressures, J. Phys. Chem. B **124**, 10500 (2020).

[78] T. D. Cuong, A. D. Phan, K. Wakabayashi, and P. T. Huy, Structural relaxation time and dynamic shear modulus of glassy graphene, J. Non-Cryst. Solids **538**, 120024 (2020).

[79] A. D. Phan, A. Zaccone, V. D. Lam, and K. Wakabayashi, Theory of pressure-induced rejuvenation and strain hardening in metallic glasses, Phys. Rev. Lett. **126**, 025502 (2021).

[80] T. D. Cuong, N. Q. Hoc, N. D. Trung, N. T. Thao, and A. D. Phan, Theoretical predictions of melting behaviors of hcp iron up to 4000 GPa, Phys. Rev. B **106**, 094103 (2022).

[81] J. K. Percus and G. J. Yevick, Analysis of classical statistical mechanics by means of collective coordinates, Phys. Rev. **110**, 1 (1958).

[82] M. S. Wertheim, Exact solution of the Percus-Yevick integral equation for hard spheres, Phys. Rev. Lett. **10**, 321 (1963).

[83] J. P. Hansen and I. R. McDonald, *Theory of Simple Liquids* (Academic Press, London, 2006).

[84] S. Khrapak, N. P. Kryuchkov, L. A. Mistryukova, and S. O. Yurchenko, From soft-to hard-sphere fluids: Crossover evidenced by high-frequency elastic moduli, Phys. Rev. E **103**, 052117 (2021).

[85] K. S. Schweizer and E. J. Saltzman, Entropic barriers, activated hopping, and the glass transition in colloidal suspensions, J. Chem. Phys. **119**, 1181 (2003).

[86] K. S. Schweizer, Derivation of a microscopic theory of barriers and activated hopping transport in glassy liquids and suspensions, J. Chem. Phys. **123**, 244501 (2005).

[87] K. S. Schweizer and G. Yatsenko, Collisions, caging, thermodynamics, and jamming in the barrier hopping theory of glassy hard sphere fluids, J. Chem. Phys. **127**, 164505 (2007).

[88] L. D. Landau and E. M. Lifshitz, *Theory of Elasticity* (Permagon Press, London, 1975).

[89] A. D. Phan, A. Jedrzejowska, M. Paluch, and K. Wakabayashi, Theoretical and experimental study of compression effects on structural relaxation of glass-forming liquids, ACS Omega **5**, 11035 (2020).

[90] A. D. Phan and K. Wakabayashi, Theory of structural and secondary relaxation in amorphous drugs under compression, Pharmaceutics **12**, 177 (2020).

[91] A. Ghanekarade, A. D. Phan, K. S. Schweizer, and D. S. Simmons, Nature of dynamic gradients, glass formation, and collective effects in ultrathin freestanding films, Proc. Natl. Acad. Sci. USA **118**, e2104398118 (2021).

[92] G. G. Stokes, On the theories of the internal friction in fluids in motion, and of the equilibrium and motion of elastic solids, Trans. Cambridge Philos. Soc. **22**, 287 (1845).

[93] A. Einstein, On the motion of small particles suspended in liquids at rest required by the molecular-kinetic theory of heat, Ann. Phys. **322**, 549 (1905).

[94] M. S. Green, Markoff random processes and the statistical mechanics of time-dependent phenomena. II. Irreversible processes in fluids, J. Chem. Phys. **22**, 398 (1954).

[95] R. Kubo, Statistical–mechanical theory of irreversible processes. I. General theory and simple applications to magnetic and conduction problems, J. Phys. Soc. Jpn. **12**, 570 (1957).

[96] M. I. Mendelev, S. Han, D. J. Srolovitz, G. J. Ackland, D. Y. Sun, and M. Asta, Development of new interatomic potentials appropriate for crystalline and liquid iron, Philos. Mag. **83**, 3977 (2003).

[97] J. Ma, W. Li, G. Yang, S. Zheng, Y. He, X. Zhang, X. Zhang, and X. Zhang, Modeling the pressure-dependent melting temperature of metals, Phys. Earth Planet. Inter. **309**, 106602 (2020).

[98] T. D. Cuong and A. D. Phan, Theoretical model for the high-pressure melting process of MgO with the B1 structure, Vacuum **189**, 110231 (2021).

[99] T. D. Cuong and A. D. Phan, Toward better understanding of the high-pressure structural transformation in beryllium by the statistical moment method, Phys. Chem. Chem. Phys. **25**, 9073 (2023).

[100] T. D. Cuong and A. D. Phan, Reconstructing the phase diagram of iron in the terapascal region via the statistical moment method, Phys. Rev. B **108**, 134111 (2023).

[101] P. Vinet, J. H. Rose, J. Ferrante, and J. R. Smith, Universal features of the equation of state of solids, J. Phys.: Condens. Matter **1**, 1941 (1989).

[102] F. A. Lindemann, Ìber die berechnung molekularer eigenfrequenzen, Phys. Z. **11**, 609 (1910).

[103] L. Burakovsky, D. L. Preston, and R. R. Silbar, Analysis of dislocation mechanism for melting of elements: Pressure dependence, J. Appl. Phys. **88**, 6294 (2000).

[104] L. J. Swartzendruber, The Fe (iron) system, Bull. Alloy Phase Diagrams **3**, 161 (1982).

[105] K. Masuda-Jindo, V. V. Hung, and P. D. Tam, Thermodynamic quantities of metals investigated by an analytic statistical moment method, Phys. Rev. B **67**, 094301 (2003).

[106] K. Masuda-Jindo, S. R. Nishitani, and V. VanHung, hcp-bcc structural phase transformation of titanium: Analytic model calculations, Phys. Rev. B **70**, 184122 (2004).

[107] T. D. Cuong and A. D. Phan, Theoretical insights into non-Arrhenius behaviors of thermal vacancies in anharmonic crystals, Phys. Chem. Chem. Phys. **24**, 4910 (2022).

[108] G. Aquilanti, A. Trapananti, A. Karandikar, I. Kantor, C. Marini, O. Mathon, S. Pascarelli, and R. Boehler, Melting of iron determined by x-ray absorption spectroscopy to 100 GPa, Proc. Natl. Acad. Sci. USA **112**, 12042 (2015).

[109] A. Basu, M. R. Field, D. G. McCulloch, and R. Boehler, New measurement of melting and thermal conductivity of iron close to outer core conditions, Geoscience Frontiers **11**, 565 (2020).

[110] J. M. Jackson, W. Sturhahn, M. Lerche, J. Zhao, T. S. Toellner, E. E. Alp, S. V. Sinogeikin, J. D. Bass, C. A. Murphy, and J. K. Wicks, Melting of compressed iron by monitoring atomic dynamics, Earth Planet. Sci. Lett. **362**, 143 (2013).

[111] D. Zhang, J. M. Jackson, J. Zhao, W. Sturhahn, E. E. Alp, M. Y. Hu, T. S. Toellner, C. A. Murphy, and V. B. Prakapenka, Temperature of Earth's core constrained from melting of Fe and $Fe_{0.9}Ni_{0.1}$ at high pressures, Earth Planet. Sci. Lett. **447**, 72 (2016).

[112] G. Morard, S. Boccato, A. D. Rosa, S. Anzellini, F. Miozzi, L. Henry, G. Garbarino, M. Mezouar, M. Harmand, F. Guyot, E. Boulard, I. Kantor, T. Irifune, and R. Torchio, Solving controversies on the iron phase diagram under high pressure, Geophys. Res. Lett. **45**, 11074 (2018).

[113] J. Li, Q. Wu, J. Li, T. Xue, Y. Tan, X. Zhou, Y. Zhang, Z. Xiong, Z. Gao, and T. Sekine, Shock melting curve of iron: A consensus on the temperature at the Earth's inner core boundary, Geophys. Res. Lett. **47**, e2020GL087758 (2020).

[114] S. J. Turneaure, S. M. Sharma, and Y. M. Gupta, Crystal structure and melting of Fe shock compressed to 273 GPa: *In situ* X-Ray diffraction, Phys. Rev. Lett. **125**, 215702 (2020).

[115] M. Hou, J. Liu, Y. Zhang, X. Du, H. Dong, L. Yan, J. Wang, L. Wang, and B. Chen, Melting of iron explored by electrical resistance jump up to 135 GPa, Geophys. Res. Lett. **48**, e2021GL095739 (2021).

[116] D. Alfe, G. D. Price, and M. J. Gillan, Iron under Earth's core conditions: Liquid-state thermodynamics and high-pressure melting curve from *ab initio* calculations, Phys. Rev. B **65**, 165118 (2002).

[117] D. Alfe, Temperature of the inner-core boundary of the Earth: Melting of iron at high pressure from first-principles coexistence simulations, Phys. Rev. B **79**, 060101(R) (2009).

[118] E. Sola and D. Alfe, Melting of iron under Earth's core conditions from diffusion Monte Carlo free energy calculations, Phys. Rev. Lett. **103**, 078501 (2009).

[119] T. Sun, J. P. Brodholt, Y. Li, and L. Vocadlo, Melting properties from *ab initio* free energy calculations: Iron at the Earth's inner-core boundary, Phys. Rev. B **98**, 224301 (2018).

[120] Z. Zhang, G. Csanyi, and D. Alfe, Partitioning of sulfur between solid and liquid iron under Earth's core conditions: Constraints from atomistic simulations with machine learning potentials, Geochim. Cosmochim. Acta **291**, 5 (2020).

[121] R. Hrubiak, Y. Meng, and G. Shen, Experimental evidence of a body centered cubic iron at the Earth's core condition, arXiv:1804.05109.

[122] F. Simon and G. Glatzel, Bemerkungen zur schmelzdruckkurve, Z. Anorg. Allg. Chem. **178**, 309 (1929).

[123] N. Dass and M. Kumari, On the isothermal Anderson-Grüneisen parameter in solids, Phys. Status Solidi B **124**, 531 (1984).

[124] L. Burakovsky, D. L. Preston, and R. R. Silbar, Melting as a dislocation-mediated phase transition, Phys. Rev. B **61**, 15011 (2000).

[125] L. Gomez, A. Dobry, Ch. Geuting, H. T. Diep, and L. Burakovsky, Dislocation lines as the precursor of the melting of crystalline solids observed in Monte Carlo simulations, Phys. Rev. Lett. **90**, 095701 (2003).

[126] G. Arfken, *Mathematical Methods for Physicists* (Academic, Orlando, 1985).

[127] L. A. Miccio, C. Borredon, U. Casado, A. D. Phan, and G. A. Schwartz, Approaching polymer dynamics combining artificial neural networks and elastically collective nonlinear Langevin equation, Polymers **14**, 1573 (2022).

[128] A. D. Phan, N. K. Ngan, D. T. Nga, N. B. Le, and C. V. Ha, Tailoring drug mobility by photothermal heating of graphene plasmons, Phys. Status Solidi RRL **16**, 2100496 (2022).

[129] A. D. Phan, Confinement effects on the spatially inhomogeneous dynamics in metallic glass films, J. Phys. Chem. B **126**, 1609 (2022).

[130] A. B. Belonoshko, P. I. Dorogokupets, B. Johansson, S. K. Saxena, and L. Koci, *Ab initio* equation of state for the body-centered-cubic phase of iron at high pressure and temperature, Phys. Rev. B **78**, 104107 (2008).

[131] Y. He, S. Sun, D. Y. Kim, B. G. Jang, H. Li, and H. K. Mao, Superionic iron alloys and their seismic velocities in Earth's inner core, Nature (London) **602**, 258 (2022).

[132] S. Sun, Y. He, J. Yang, Y. Lin, J. Li, D. Y. Kim, H. Li, and H. K. Mao, Superionic effect and anisotropic texture in Earth's inner core driven by geomagnetic field, Nat. Commun. **14**, 1656 (2023).

[133] P. Lunkenheimer, A. Loidl, B. Riechers, A. Zaccone, and K. Samwer, Thermal expansion and the glass transition, Nat. Phys. **19**, 694 (2023).

[134] K. Grzybowska, S. Capaccioli, and M. Paluch, Recent developments in the experimental investigations of relaxations in pharmaceuticals by dielectric techniques at ambient and elevated pressure, Adv. Drug Delivery Rev. **100**, 158 (2016).

[135] Y. Nishihara, S. Doi, N. Tsujino, D. Yamazaki, K. N. Matsukage, Y. Tsubokawa, T. Yoshino, A. R. Thomson, Y. Higo, and Y. Tange, Rheology of hexagonal close-packed (hcp) iron, J. Geophys. Res.: Solid Earth **128**, e2022JB026165 (2023).

[136] Q. Li, T. Sun, Y. G. Zhang, J. W. Xian, and L. Vocadlo, Atomic transport properties of liquid iron at conditions of planetary cores, J. Chem. Phys. **155**, 194505 (2021).

[137] D. Ikuta, E. Ohtani, H. Fukui, T. Sakai, D. Ishikawa, and A. Q. R. Baron, Sound velocity of hexagonal close-packed iron to the Earth's inner core pressure, Nat. Commun. **13**, 7211 (2022).

[138] B. Martorell, J. Brodholt, I. G. Wood, and L. Vocadlo, The elastic properties and stability of fcc-Fe and fcc-FeNi alloys at inner-core conditions, Geophys. J. Int. **202**, 94 (2015).

[139] Z. Li and S. Scandolo, Elasticity and viscosity of hcp iron at Earth's inner core conditions from machine learning-based large-scale atomistic simulations, Geophys. Res. Lett. **49**, e2022GL101161 (2022).

[140] A. M. Dziewonski and D. L. Anderson, Preliminary reference Earth model, Phys. Earth Planet. Inter. **25**, 297 (1981).

[141] B. L. N. Kennett, E. R. Engdahl, and R. Buland, Constraints on seismic velocities in the Earth from traveltimes, Geophys. J. Int. **122**, 108 (1995).

[142] T. Costa de Lima, T. S. Pham, X. Ma, and H. Tkalcic, An estimate of absolute shear-wave speed in the Earth's inner core, Nat. Commun. **14**, 4577 (2023).

[143] L. Stixrude, Melting in super-earths, Philos. Trans. R. Soc. London A **372**, 20130076 (2014).

[144] A. Boujibar, P. Driscoll, and Y. Fei, Super-Earth internal structures and initial thermal states, J. Geophys. Res.: Planets **125**, e2019JE006124 (2020).

[145] J. Zhang and L. A. Rogers, Thermal evolution and magnetic history of rocky planets, Astrophys. J. **938**, 131 (2022).
[146] I. N. Sneddon and D. S. Berry, *The Classical Theory of Elasticity* (Springer, Berlin, 1958).
[147] S. Wang and H. Tkalcic, Shear-wave anisotropy in the Earth's inner core, Geophys. Res. Lett. **48**, e2021GL094784 (2021).
[148] W. Voigt, Ueber die Beziehung zwischen den beiden Elasticitätsconstanten isotroper Körper, Ann. Phys. **274**, 573 (1889).
[149] A. Reuss, Berechnung der fließgrenze von mischkristallen auf grund der plastizitätsbedingung für einkristalle, Z. Angew. Math. Mech. **9**, 49 (1929).
[150] R. Hill, The elastic behaviour of a crystalline aggregate, Proc. Phys. Soc. London, Sect. A **65**, 349 (1952).
[151] H. Tkalčić, S. Wang, and T. S. Pham, Shear properties of Earth's inner core, Annu. Rev. Earth Planet Sci. **50**, 153 (2022).
[152] R. Widmer, G. Masters, and F. Gilbert, Spherically symmetric attenuation within the Earth from normal mode data, Geophys. J. Int. **104**, 541 (1991).
[153] J. Resovsky, J. Trampert, and R. D. Van der Hilst, Error bars for the global seismic Q profile, Earth Planet. Sci. Lett. **230**, 413 (2005).
[154] R. W. L. de Wit, P. J. Kaufl, A. P. Valentine, and J. Trampert, Bayesian inversion of free oscillations for Earth's radial (an)elastic structure, Phys. Earth Planet. Inter. **237**, 1 (2014).
[155] S. Talavera-Soza and A. Deuss, Constraining 1-D inner core attenuation through measurements of strongly coupled normal mode pairs, Geophys. J. Int. **223**, 612 (2020).
[156] A. Deuss, J. H. Woodhouse, H. Paulssen, and J. Trampert, The observation of inner core shear waves, Geophys. J. Int. **142**, 67 (2000).
[157] J. Wookey and G. Helffrich, Inner-core shear-wave anisotropy and texture from an observation of PKJKP waves, Nature (London) **454**, 873 (2008).
[158] A. Cao and B. Romanowicz, Constraints on shear wave attenuation in the Earth's inner core from an observation of PKJKP, Geophys. Res. Lett. **36**, L09301 (2009).
[159] H. Tkalčić and T. S. Pham, Shear properties of Earth's inner core constrained by a detection of *J* waves in global correlation wavefield, Science **362**, 329 (2018).
[160] I. Sumita, S. Yoshida, M. Kumazawa, and Y. Hamano, A model for sedimentary compaction of a viscous medium and its application to inner-core growth, Geophys. J. Int. **124**, 502 (1996).
[161] J. W. Xian, T. Sun, and T. Tsuchiya, Viscoelasticity of liquid iron at conditions of the Earth's outer core, J. Geophys. Res.: Solid Earth **124**, 11105 (2019).
[162] M. Lasbleis, M. Kervazo, and G. Choblet, The fate of liquids trapped during the Earth's inner core growth, Geophys. Res. Lett. **47**, e2019GL085654 (2020).
[163] G. Leibfried and W. Ludwig, Theory of anharmonic effects in crystals, Solid State Phys. **12**, 275 (1961).
[164] Q. Ye, Y. Hu, X. Duan, H. Liu, H. Zhang, C. Zhang, L. Sun, W. Yang, W. Xu, Q. Cai, Z. Wang, and S. Jiang, Theoretical development and experimental validation on the measurement of temperature by extended x-ray absorption fine structure, J. Synchrotron Radiat. **27**, 436 (2020).
[165] N. Tang and V. V. Hung, Investigation of the thermodynamic properties of anharmonic crystals by the momentum method. I. General results for face-centred cubic crystals, Phys. Status Solidi B **149**, 511 (1988).
[166] V. V. Hung, K. Masuda-Jindo, and P. T. M. Hanh, Application of the statistical moment method to thermodynamic quantities of silicon, J. Phys.: Condens. Matter **18**, 283 (2006).
[167] D. D. Phuong, N. T. Hoa, V. V. Hung, D. Q. Khoa, and H. K. Hieu, Mechanical properties of metallic thin films: theoretical approach, Eur. Phys. J. B **89**, 84 (2016).
[168] H. T. T. Vu, H. T. M. Pham, T. V. Nguyen, and H. K. Ho, Pressure effects on the thermodynamic and mechanical properties of zinc-blende ZnTe compound, Eur. Phys. J. B **90**, 65 (2017).